Mon. Not. R. astr. Soc. (1987) **226,** 655–687

The statistics of cosmic background radiation fluctuations

J. R. Bond *Canadian Institute for Theoretical Astrophysics, Toronto, ON M5S 1A1, Canada*

G. Efstathiou *Institute of Astronomy, Madingley Road, Cambridge CB3 0HA and Institute for Advanced Study, Princeton, NJ 08540, USA*

Accepted 1987 January 9. Received 1986 November 25

Summary. We present computations of the radiation correlation functions and angular power spectra for microwave background anisotropies expected in $\Omega=1$ cold dark matter dominated universes with scale-invariant adiabatic or isocurvature initial conditions. The results are valid on all angular scales. We describe the statistical properties of the radiation pattern and develop the theory of two-dimensional Gaussian random fields. A large number of properties of such fields may be derived analytically or semi-analytically, such as the number densities of hotspots and coldspots, the eccentricities of peaks and peak correlation properties. The formulae presented here provide valuable insight into the textural characteristics of the microwave background anisotropies and must be satisfied if the primordial fluctuations are Gaussian. The assumption of Gaussian initial conditions allow us to make highly specific predictions for the pattern of the temperature anisotropies. This is demonstrated by the construction of maps of the fluctuations predicted for the total intensity and the polarization.

1 Introduction

The origin of density irregularities in the Universe represents one of the most important problems in cosmology which, until recently, was largely considered intractable. The inflationary model of the early Universe has, however, led to a potentially viable mechanism for the origin of primordial density fluctuations (e.g. Starobinskii 1982; Guth & Pi 1982; Bardeen, Steinhardt & Turner 1983). Although these calculations are hardly definitive, they have succeeded in drawing attention to a particular set of initial conditions, namely scale-invariant, Gaussian fluctuations superimposed on an $\Omega=1$ Friedman background.

In this paper, we investigate the statistical properties of the cosmic microwave background radiation (CMB), assuming that the initial fluctuations are Gaussian. The background radiation will then form a 2D Gaussian random field and should provide a clean and direct test of the statistics of the initial conditions. Given a particular cosmological model, we can compute all statistical aspects of the radiation pattern. It is unfortunate, then, that CMB anisotropies have yet

to be detected, for they would provide a definitive test of the inflationary prediction of scale-invariant Gaussian fluctuations.

The general predictions of the inflationary picture, together with constraints derived from primordial nucleosynthesis (Yang *et al.* 1984), observations and simulations of galaxy clustering (Davis & Peebles 1983; White, Frenk & Davis 1983; Davies *et al.* 1985) and CMB anisotropies (Bond & Efstathiou 1984; Vittorio & Silk 1984) have in turn led to a serious candidate model for the origin of large-scale structure in which the present mass density is dominated by cold dark matter (CDM, see the review by Blumenthal *et al.* 1984, and references therein). The favoured set of parameters for the CDM model, consistent with the above constraints, are as follows: (i) adiabatic, Gaussian, scale-invariant initial conditions; (ii) $\Omega=1$, $\Lambda=0$; (iii) $h=(H_0/100\,\mathrm{km\,s^{-1}\,Mpc^{-1}})\approx 0.5$; (iv) baryon density $\Omega_B\approx 0.1$.

Here we present a thorough analysis of the CMB anisotropies expected in $\Omega=1$ CDM models. The high level of detail of our study is motivated by our impression that there is a realistic prospect of detecting the CMB anisotropies in the near future if the CDM model with the parameters listed above is correct. For example, a beam-switching experiment with a beam throw of 6° and a Gaussian beam profile of 5° FWHM [similar to the experimental configuration of Melchiorri *et al.* (1981) who report a detection of $\Delta T/T=4.1\pm 0.7\times 10^{-5}$] would yield $\langle(\Delta T/T)^2\rangle^{1/2}=1.2\times 10^{-5}/b$ (Section 4.1). Here b is a 'biasing' parameter which is unity if galaxies trace the mass distribution and is expected to lie in the range 1.5–2.5 in this specific model (Section 4.3). In the absence of beam smearing, the predicted anisotropy on this angular scale is $4.7\times 10^{-5}/b$. We have provided the results of our computations in a form in which experimenters can readily assess the level of sensitivity required of their particular experimental configuration to set convincing constraints on the CDM model.

If primordial CMB anisotropies are discovered at about the level suggested above, then attention will shift towards much more demanding tests of the model, such as the shape of the radiation correlation function and tests of the Gaussian nature of the initial conditions. We have therefore emphasized the spatial characteristics of the radiation field throughout this paper and have provided examples of how the fluctuations would appear in the sky. Full information on the temperature autocorrelation function can only be obtained by mapping sizeable regions of the celestial sphere. In many respects, such studies of the CMB will be similar to current investigations of large-scale structures in the galaxy distribution. In the case of the CMB there is a reasonable hope that non-linear effects are unimportant (at least on scales >1 arcmin, Ostriker & Vishniac 1986) though this simplicity is partly offset by the difficulty of the observations.

In Section 2, we discuss the general formulation of the statistical problem for the CMB. We assume that the radiation field is Gaussian, hence entirely characterized by the two-point angular correlation function $C(\theta)$ or its angular power spectrum. In Section 3, we present a short summary of the mathematical theory of the texture of maxima and minima in 2D homogeneous and isotropic Gaussian random fields, presenting results for their number density and separations, their shapes, and their correlation functions. The development of these results is relegated to four appendices, and relies heavily on the theory of peaks for 3D random fields as developed by Bardeen *et al.* (1986, hereafter BBKS). These results provide a number of requirements which the radiation field must necessarily satisfy if it is Gaussian.

In independent work, Sazhin (1985) and Zabotin & Nasel'skii (1985) have also considered some of the properties of hotspots and coldspots. These authors have suggested that experiments may be capable of detecting high peaks in the radiation intensity fluctuations even if they are insensitive (i.e. noise limited) to more typical 1σ fluctuations. However, peaks of height 3σ and higher are extremely rare. Further, if instrumental/confusion noise has spatial characteristics similar to those of intrinsic CMB fluctuations, it will be difficult to distinguish between high peaks in the radiation field and rare excursions in the noise. However, if noise is correlated only on small

scales, then the spatial characteristics of the intrinsic fluctuations may be recovered by applying a low pass filter. We stress that at this stage the primary use of our statistical analysis is as a device to aid intuition, since armed with only two numbers (the parameters γ and θ_* defined in Section 2.4 below) a variety of interesting features of the radiation pattern may easily be computed.

In Section 4, we describe the formalism for detailed calculations of $C(\theta)$ and related spectral parameters which we apply to adiabatic and isocurvature CDM universes with scale-invariant initial conditions. The techniques are generally applicable, however, and are not specific to this class of models. In Section 5, we display realizations of the radiation pattern expected in two $\Omega=1$ CDM models of the Universe and compare these with some of the results of Section 3. Our main results are summarized in Section 6.

2 Radiation fluctuation statistics

In this section, we first discuss how the statistical distribution of the initial fluctuations translates into an equivalent distribution for the microwave background radiation pattern, provided that the Universe is linear at the epochs at which the CMB fluctuations arise. We then introduce the single quantity required to specify the Gaussian statistics of the radiation pattern, $C(\theta)$, and the associated angular power spectrum (Section 2.2). In Section 2.3, the finite beam size of radio telescopes is shown to be equivalent to low pass filtering of the power spectrum. Spectral parameters required to describe the properties of the maxima and minima and the overall amplitude of the radiation fluctuations are defined in Section 2.4.

2.1 GAUSSIAN STATISTICS

We assume that the initial perturbations form a Gaussian random field. As mentioned in the introduction, this hypothesis has been adopted in many popular models of galaxy formation, in particular in those relying on fluctuation generation in an inflationary epoch. In inflationary models, adiabatic and isocurvature perturbations may arise from quantum mechanical fluctuations of a scalar field in de Sitter space (e.g. Bardeen *et al.* 1983; Axenides, Brandenberger & Turner 1983). Provided that the scalar field spatial fluctuations can be treated as linear perturbations to the dominant spatially homogeneous component of the scalar field, then the perturbation acts like a free quantum field with zero-point oscillations in the de Sitter vacuum described by a Gaussian wave functional (Fischler, Ratra & Susskind 1985; Halliwell & Hawking 1985). When translated to a classical random field description, the probability functional, the square of the wave functional, is Gaussian in each of the scalar field modes with random phases.

As long as the fluctuations obey linear evolution equations, the joint probability distribution for any number of the normal modes of the perturbations is form-invariant: N-point correlation functions of normal mode amplitudes evolve in a self-similar way. Only when mode–mode coupling occurs in the non-linear regime does the form of these probability functionals change. In particular Gaussian fields remain Gaussian throughout the linear regime. (This is also the case for fields whose normal modes have random phases, for the central limit theorem implies that such fields obey Gaussian statistics to a high degree of precision.)

We define the fluctuations Δ_T in the microwave background by the perturbation to the photon distribution function:

$$\delta f_T(\mathbf{q}, \mathbf{x}, \tau) \equiv (T_0 \partial \bar{f}/\partial T_0)\, \Delta_T(\hat{q}, \mathbf{x}, \tau)/4.$$

Here, T_0 and $\bar{f}$ are the unperturbed radiation temperature and distribution function, respectively, $\hat{q}$ is a unit vector in the direction of the photon momentum $\mathbf{q}$, $\mathbf{x}$ is the comoving position and τ is conformal time, $\int dt/a(t)$ where a is the cosmological scale factor.

Since we assume that the fluctuations in the microwave background were imprinted in the linear regime, Δ_T will be a linear combination of the initial perturbation amplitudes, and will

therefore have the same probability distribution. In particular, $\Delta_T(\hat{q})$ evaluated at our current location $\mathbf{x}=0$ and epoch $\tau=\tau_0$, the *two-dimensional* field which the experiments probe, is Gaussian if the initial conditions are. Such fields with zero mean are completely characterized by their two-point correlation functions, or equivalently, their power spectra. The radiation correlation function,

$$C(\theta)\equiv \tfrac{1}{16}\langle \Delta_T(\hat{q}_1)\,\Delta_T(\hat{q}_2)\rangle \qquad \cos(\theta)\equiv \hat{q}_1\cdot\hat{q}_2, \tag{2.1}$$

depends only upon the relative angle θ and not on the absolute directions of the incoming photons. This is a consequence of homogeneity and isotropy.

2.2 POWER SPECTRUM

The CMB radiation pattern represents a 2D random field on the two-sphere. A Gaussian random field in a rectangular domain is completely characterized by the Fourier components of the two-point correlation function, its power spectrum. The analogue in spherical geometry is C_l, the lth component of the Legendre polynomial expansion:

$$C(\theta)=\frac{1}{4\pi}\sum_l (2l+1)\,C_l P_l(\cos\theta). \tag{2.2}$$

The discrete function C_l is the power spectrum associated with a spherical harmonic expansion of the radiation temperature seen on the sky from our location:

$$\begin{aligned} T(\hat{q}) &\equiv T_0[1+\Delta_T(\hat{q},\ \mathbf{x}=0,\ \tau_0)/4] \\ &\equiv T_0\sum_{lm} a_l^m Y_l^m(\hat{q}). \end{aligned} \tag{2.3}$$

For Gaussian fields, the spherical harmonic expansion coefficients a_l^m, $l\neq 0$, are independent Gaussian fields with random phases, zero means, and variances

$$\langle a_l^m a_{l'}^{m'}\rangle=\delta_{ll'}\delta_{mm'}C_l, \qquad l\neq 0. \tag{2.4}$$

The monopole Gaussian variable $a_0^0/(4\pi)^{1/2}$ has mean 1 and dispersion C_0. However, since the average microwave background temperature we observe,

$$\bar{T}=T_0\left(1+\int\frac{d\Omega}{4\pi}\Delta_T/4\right)=T_0 a_0^0/(4\pi)^{1/2}, \tag{2.5}$$

includes the monopole part of the perturbation, the $'\Delta T/T'$ we would measure is $(T-\bar{T})/\bar{T}$ with the monopole subtracted off. In addition, the large dipole component

$$\sum a_1^m Y_1^m \equiv \mathbf{d}\cdot\hat{q},$$

which is most likely due to our motion ($\mathbf{d}\approx \mathbf{v}/c$), should be subtracted before a correlation function is determined. The sum in equation (2.2) is therefore restricted to $l\geq 2$ terms.

The correlation function measured from our position will differ from the ensemble average equation (2.1). The observed correlation function $C_{\rm obs}$ could, with complete observational information, be determined by angle-averaging $\Delta T(\hat{q})\,\Delta T(\hat{q}')$ over the sky with $|\hat{q}-\hat{q}'|$ kept fixed:

$$C_{\rm obs}(\theta)=\sum_{l\geq 2}\sum_{m=-l}^{l}|a_l^m|^2/(4\pi)\,P_l(\hat{q}\cdot\hat{q}'). \tag{2.6}$$

Within the ensemble, $C_{\rm obs}$ has a non-Gaussian probability distribution with mean given by the ensemble average, equation (2.2), but with a variance

$$\langle[C_{\rm obs}(\theta)-C(\theta)]^2\rangle=\left(\frac{1}{4\pi}\right)^2\sum_l (2l+1)\,C_l^2\,P_l^2$$

about that mean. The contribution to the sum over l for modes with comoving wavenumber k, is dominated by terms with $l \sim k\tau_0$. The relative deviation of realization average from ensemble average is therefore $\sim(k\tau_0)^{-1/2}$, negligible unless there is a large amount of power on horizon-scale wavelengths. However, this is precisely the case for the model universes which are currently of most interest, those with scale-invariant initial fluctuations having equal power per decade on scales larger than the horizon at recombination. The shape of $C(\theta)$ will then be difficult to determine reliably at any angular scale unless a large-angle high pass filter is first applied to the map. Accordingly tests of theoretical predictions will require careful modelling of the estimation techniques, an issue we turn to again in Section 6.

For small angular patches of the sky, a framework more closely aligned to that used for Gaussian fields in flat 2D space is more appropriate. Consider the region about an arbitrarily chosen 'North Pole' of the sky. Choose polar coordinates (ϖ, ϕ) about this pole where ϕ is longitude, $\varpi = 2\sin(\theta/2)$, and θ colatitude. The constraint $\varpi < 2$ gives an equal area mapping of a disc of radius 2 on to the two-sphere ($d\Omega = \varpi\, d\varpi\, d\phi$, with $d\Omega$ a solid angle element). The map is extremely distorted near the South Pole, the $\varpi = 2$ boundary. For $\varpi \ll 2$, the geometry is flat. If we define a continuous power spectrum of $C(\theta)$ by

$$S(Q) = 2\pi \int_0^2 \varpi\, d\varpi\, C(\varpi)\, J_0(Q\varpi), \tag{2.7a}$$

the Fourier transform of $C(\theta)\vartheta(2-\varpi)$, with ϑ denoting the Heaviside function, then

$$C(\theta) = (2\pi)^{-1} \int_0^\infty Q\, dQ\, S(Q)\, J_0(Q\varpi). \tag{2.7b}$$

Provided CJ_0 falls off sufficiently rapidly with ϖ, we can take the upper range of the integral in equation (2.7a) to be infinite, so C and S form a Hankel transform pair.

In the limit of large l and small ϖ, $P_l(\cos\theta) \approx J_0[(l+\tfrac{1}{2})\theta]$, hence

$$S(Q) \approx C_l, \qquad Q \approx l \gg 1. \tag{2.8}$$

Thus C_l can be used in the construction of maps of small patches of the sky by Fourier transforms, a prescription we use in Section 5.

2.3 BEAM PROFILE FILTERING

The finite beam size of a radio telescope may be taken into account by convolving the intensity with a resolution function $\mathscr{F}(\hat{q}-\hat{q}')$, where $\hat{q}$ denotes the beam centre and $-\hat{q}'$ denotes the directions of arrival of the photons incident on the telescope:

$$\Delta_{\mathrm{T}}^{\mathscr{F}}(\hat{q}) \equiv \Delta_{\mathrm{T}}(\hat{q};\theta_{\mathrm{s}}) = \int d\Omega_{\hat{q}'}\, \mathscr{F}(\hat{q}-\hat{q}')\, \Delta_{\mathrm{T}}(\hat{q}'). \tag{2.9}$$

Some telescopes have asymmetric convolution functions which are quite complicated, though, in most cases, $\mathscr{F}$ is approximately symmetric. The full-width at half-maximum θ_{fwhm} is the scale most often used to characterize the beam smearing. Instead, we use a *smoothing angle*

$$\theta_{\mathrm{s}} \equiv 0.425\, \theta_{\mathrm{fwhm}} \tag{2.10}$$

to characterize the beam-smearing scale, motivated by the Gaussian approximation to the smoothing function $\mathscr{F}$:

$$\mathscr{F}(\hat{q}-\hat{q}') = \frac{1}{2\pi\theta_{\mathrm{s}}^2} \exp[-|\hat{q}-\hat{q}'|^2/(2\theta_{\mathrm{s}}^2)]. \tag{2.11}$$

If $\mathscr{F}$ is a function only of $|\hat{q}-\hat{q}'|$, then it can be expanded in Legendre polynomials with

coefficients $\mathscr{F}_l/(4\pi)$ as in equation (2.2); alternatively we can determine the Fourier transform $\tilde{\mathscr{F}}(Q)$ of $\mathscr{F}$ using the polar coordinate prescription of equation (2.7a). The beam-smeared correlation function is then

$$C(\theta;\theta_s)=\frac{1}{4\pi}\sum_l (2l+1)\,\mathscr{F}_l^2 C_l P_l(\cos\theta)$$

$$\approx\int\frac{Q\,dQ}{2\pi}|\tilde{\mathscr{F}}(Q)|^2\,S(Q)\,J_0(Q\varpi)$$

$$=\int_0^2\exp\left[-\frac{(\varpi^2+\varpi_1^2)}{4\theta_s^2}\right]I_0\left(\frac{\varpi\varpi_1}{2\theta_s^2}\right)C(\varpi_1)\,\frac{\varpi_1\,d\varpi_1}{2\theta_s^2}. \tag{2.12}$$

The first two expressions clearly show that $\mathscr{F}$ acts as a filter on the power spectrum whether we work in l or Q space. The last expression holds for Gaussian profiles (Wilson & Silk 1981), for which

$$\mathscr{F}_l\approx\tilde{\mathscr{F}}(Q)=\exp(-\theta_s^2Q^2/2). \tag{2.13}$$

2.4 SPECTRAL PARAMETERS

In addition to filtering by finite beam resolution, there are physical filtering processes which damp the high Q part of the power spectrum. The associated scale is characterized by the *coherence angle*, θ_c, defined in terms of the unsmoothed correlation function,

$$\theta_c^{-2}\equiv -C''(0)/C(0), \tag{2.14}$$

where the primes denote differentiation with respect to ϖ.

Following BBKS, we define the following spectral quantities

$$\sigma_p^2(\theta_s)=\sigma_0^2\langle Q^{2p}\rangle\equiv\int_0^\infty\frac{Q\,dQ}{2\pi}Q^{2p}\,S(Q)=p!\,2^{2p}(-1)^p\frac{d^pC}{d(\varpi^2)^p}(0),$$

$$\gamma(\theta_s)\equiv\sigma_1^2/(\sigma_0\sigma_2),\qquad\theta_*(\theta_s)\equiv\sqrt{2}\sigma_1/\sigma_2. \tag{2.15}$$

In particular,

$$\sigma_0(\theta_s)=[C(0;\theta_s)]^{1/2} \tag{2.16}$$

is the overall amplitude of the rms fluctuations that would be measured in a single beam of smoothing scale θ_s. The amplitude $\sigma_0(0)$ is directly related to the correlations in the mass density, and is typically fixed by comparing with observations of galaxy correlations (BE and Section 4.2). We also define a scaled correlation function

$$\psi(\theta;\theta_s)\equiv C(\theta;\theta_s)/C(0;\theta_s) \tag{2.17}$$

which is independent of the normalization. For Gaussian beams, the rms amplitude changes with smoothing angle according to

$$\sigma_0^2(\theta_s)/\sigma_0^2(0)=\int_0^2\exp(-y)\,\psi(2\theta_s\sqrt{y})\,dy. \tag{2.18}$$

3 The statistics of hotspots and coldspots

In this section, we give an overview of the properties of the maxima and minima of 2D

homogeneous, isotropic Gaussian random fields. We relegate all of the detailed derivations and most of the relevant formulae to a series of appendices (1–4) and just highlight the results in this section. The framework we use follows closely the techniques developed by BBKS for 3D Gaussian fields. Application of some of these results to specific CDM models is given in Section 5.

The basic 2D peak problem on the sphere is to determine all of the statistical properties of the point process defined by the number density 'operator'

$$n_{\rm pk}=\sum_p \delta(\hat{q}-\hat{q}_{\rm p}) \tag{3.1}$$

for points $\hat{q}_{\rm p}$ selected to be a subclass of the extremal points of the field $[\nabla\Delta_{\rm T}(\hat{q}_{\rm p})=0]$. Additional constraints may include requiring the points to be maxima or minima, thereby restricting the range of second derivatives, to have specified amplitudes, eccentric shapes, or to lie in regions which are warmer or cooler than average when smoothed on large angles. The properties of maxima and minima on the two-sphere do not depend upon the fact that the geometry is curved rather than flat since they are defined by local properties. [The derivations of Appendix 1 do utilize an orthogonal coordinate system, which we can locally take to be the variables $(\varpi\cos\phi, \varpi\sin\phi)$ expressed in terms of the polar coordinates introduced in Section 2.] In two dimensions, the ensemble average of $n_{\rm pk}$ and of the local shapes of the radiation field about the peak points can be determined analytically, but computation of the exact two-point and higher correlation functions is difficult and we have resorted to approximate procedures. In the following, we characterize the relative heights of the radiation field by $\nu\equiv\Delta_{\rm T}/(4\sigma_0)$. Properties of hotspots and coldspots depend only upon the spectral parameters γ and θ_* and not upon the overall amplitude σ_0.

3.1 AVERAGE NUMBER DENSITY OF HOTSPOTS AND COLDSPOTS

The differential number of maxima per steradian with height in the range ν to $\nu+d\nu$ can be calculated analytically [equation (A1.9)] and the results are shown in Fig. 1(a) for a variety of γ. Only for high peaks ($\nu>3$) is the asymptotic result,

$$N_{\rm max}(\nu)\,d\nu=\frac{1}{2\pi\theta_*^2}\exp(-\nu^2/2)\frac{d\nu}{(2\pi)^{1/2}}\gamma^2(\nu^2-1)\qquad \text{as } \nu\to\infty, \tag{3.2}$$

accurate.

The integrated number density of maxima with height ν above some (sharp) threshold $\nu_{\rm t}$ (Fig. 1b) must be evaluated numerically, but is approximately given by

$$n_{\rm max}(\nu_{\rm t})=\frac{1}{4\pi\sqrt{3}\theta_*^2}\max\left[1,\left(\frac{6}{\pi}\right)^{1/2}\gamma^2\nu_{\rm t}\exp(-\nu_{\rm t}^2/2)+\operatorname{erfc}\left\{\frac{\nu_{\rm t}}{[2(1-2\gamma^2/3)]^{1/2}}\right\}\right], \tag{3.3}$$

an expression which is very accurate for $\gamma\nu>0.5$. The first term gives the number of maxima of arbitrary height ($\nu_{\rm t}=-\infty$) and the second is the analytic expression for the density of maxima plus minima, $n_{\rm max}(\nu_{\rm t})+n_{\rm min}(\nu_{\rm t})$. Of course, $n_{\rm min}(\nu_{\rm t})=n_{\rm max}(-\nu_{\rm t})$ relates the number of coldspots below a given negative threshold to the number of hotspots above the same threshold but with opposite sign. Fig. 1(c) demonstrates the accuracy of equation (3.3).

3.3 SIZE OF A HOTSPOT

Fig. 1(c) also plots the mean number density of upcrossing points $n_{\rm up}(\nu_{\rm t})$ on the contour curves $\nu=\nu_{\rm t}$ of height $\nu_{\rm t}$ [equation (A1.13)]. An upcrossing point is defined by fixing a direction and considering points on the contour curves whose tangents are perpendicular to the chosen axis and from which movement in the positive direction takes one into the contour region. For high $\nu_{\rm t}$, the

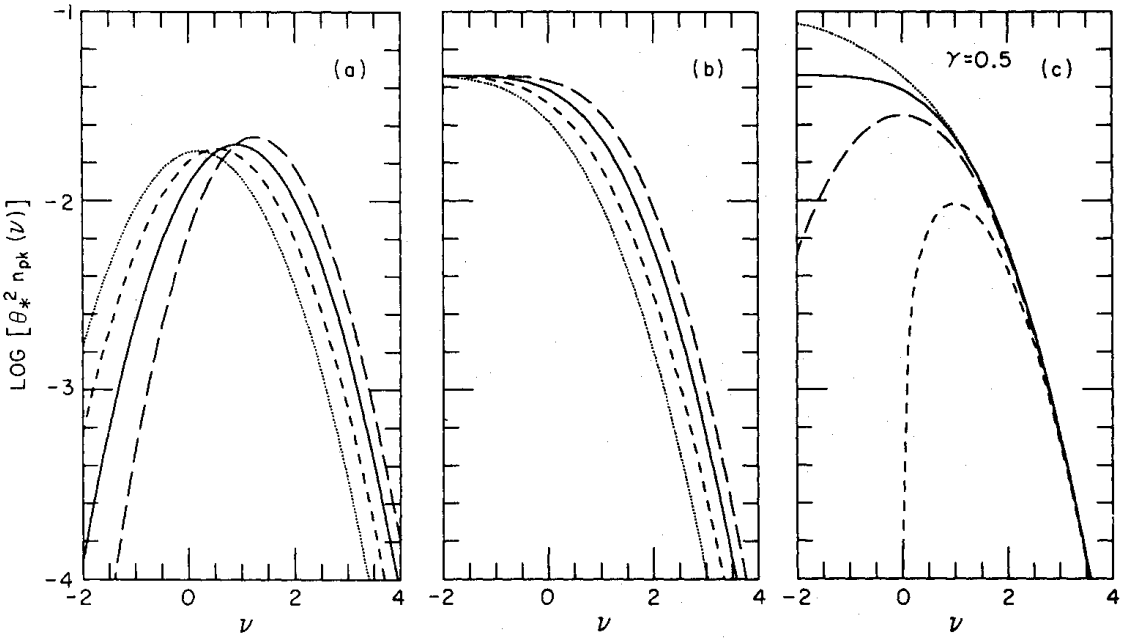

Figure 1. (a) The differential number density $\mathcal{N}_{\max}(\nu)=\mathcal{N}_{\min}(-\nu)$ is plotted against height $\nu=F/\sigma_0$ for the following values of γ: 0.1 (dot), 0.3 (short dash), 0.5 (solid), 0.7 (long dash). (b) Gives the integrated number densities $n_{\max}(\nu_t)=n_{\min}(-\nu_t)$ of peaks above the threshold ν. For $\gamma=0.5$, the density of maxima plus minima above height ν (dot), the density of upcrossing points on contour surfaces of height ν (long dash) and one-half of the Euler characteristic of these surfaces per unit area (short dash), $n_\chi/2$, are compared with the density of maxima (solid) in (c). The approximation $\max[(4.665\theta_*)^{-2}, n_{\min}+n_{\max}]$ is a good analytic approximation to $n_{\max}$ which is very accurate for $\gamma\nu>0.5$.

upcrossing points basically count the connected contour regions. For lower ν_t, the contours are highly convoluted regions so there are many upcrossing points per connected region. However, the number of upcrossing points gives an indication of the number of convex pieces within these connected regions, and hence might still be considered a reasonable measure of spot number.

The fraction of the sky enclosed within the contour regions is the probability $P(\nu>\nu_t)=0.5\,\mathrm{erfc}\,(\nu_t/\sqrt{2})$, so the area per hotspot is approximately the ratio

$$\text{Area}\ (\nu_t) \equiv \frac{P(\nu>\nu_t)}{n_{\rm up}(\nu_t)}$$

$$\sim 2\pi\left(\frac{\theta_*}{\gamma\nu_t}\right)^2\left(1-\frac{1}{\nu_t^2}\right) \qquad \text{as } \nu_t\to\infty. \tag{3.4}$$

3.3 DISTANCES BETWEEN HOTSPOTS AND COLDSPOTS

The mean distance of a hotspot of height above ν_t from a field point uncorrelated with it is

$$\langle b\,|\max,\nu_t\rangle = 2[\pi n_{\max}(\nu_t)]^{-1/2}/3. \tag{3.5}$$

For maxima of arbitary height, this mean distance is $1.8\theta_*$. Since the positions of maxima and minima are correlated, this estimate will only be an approximation to the mean distance between minima and maxima, but is a reasonable first guess. The mean distance from one peak to another does depend upon the peak–peak correlation function since high peaks tend to be strongly clustered (Section 3.5), although they do exclude each other from their immediate presence

(Bardeen *et al.*, in preparation). The net effect should reduce slightly the estimate of equation (3.5).

3.4 THE SHAPES OF HOTSPOTS AND COLDSPOTS

Local shape parameters of a peak of height, ν, measuring radial curvature, x, and asymmetry, e, are defined by the Taylor series expansion of the field about the peak taken to be at the origin of polar coordinates:

$$\Delta_T(\varpi)\approx\sigma_0\left\{\nu-\tfrac{1}{2}\gamma x\left(\frac{\varpi}{\theta_c}\right)^2\left[1+2e\cos(2\phi)\right]\right\}. \tag{3.6}$$

The contour curves in the neighbourhood of the peak are ellipses. The coordinates are orientated along the major and minor axes. The distribution of x subject to the constraint that the peak has height ν is given by equation (A2.2) and plotted in Fig. 2(a). The distributions of the 'ellipticity' e and the eccentricity $\varepsilon\equiv 2[e/(1+2e)]^{1/2}$ of the contour ellipses [equations (A2.3), (A2.5), (A2.6)] plotted in Fig. 2 show that the peaks of low height are quite elongated, and that even relatively high peaks are not circular. The average shape of the radiation field and the dispersion about this average as one goes away from the peak characterized by the constraints of given ν, ε and x [equations (A2.7) and (A2.8)] are shown in Fig. 3 for a high ($\nu=3$, $\varepsilon=0.68$) and low ($\nu=1$, $\varepsilon=0.76$) peak with average parameters appropriate to their height. The elongation of peak regions is certainly evident in the maps of Section 5 below. The cross-correlation function for unorientated peaks of height in excess of a threshold value ν_t with the temperature field is the mean profile [equation (A2.9)]

$$C_{pk,\Delta}(\theta)=\sigma_0\left[\frac{\langle\nu\rangle}{1-\gamma^2}(\psi+\theta_*^2\nabla^2\psi/2)-\frac{(\langle x\rangle/\gamma)}{1-\gamma^2}(\gamma^2\psi+\theta_*^2\nabla^2\psi/2)\right]. \tag{3.7}$$

3.5 THE HOTSPOT CORRELATION FUNCTION

Just as in the 3D case, calculation of the 2D correlation function of peaks $C_{pk,pk}(\varpi)$ above the threshold height ν_t is difficult. In Appendix 4, we resort to an approximation used in BBKS which should give good estimates for the correlation of peaks for $\varpi>\max(\theta_c,\theta_s)$, provided derivatives of $C(\theta)$ can be neglected in comparison with $C(\theta)$. The correlation function [equation (A4.10)] reduces in the limit of small ψ to

$$C_{pk,pk}(\theta)\approx\exp[A(\nu_t)\psi(\varpi)]-1, \qquad \text{for } \psi\ll 1, \tag{3.8}$$

where the amplitude $A(\nu_t)$, determined by equation (A4.15), reduces to ν_t^2 for extremely high thresholds. In addition to the continuous function equation (3.8), there is a Poisson contribution to the correlation function, $n_{pk}^{-1}(\nu_t)\delta(\hat{q}-\hat{q}')$, associated with the self-correlation of individual peaks with themselves. Further, if the continuous part of the correlation function is computed more accurately, one finds that $C_{pk,pk}$ goes to zero at $\theta=0$ reflecting the fact that different peaks are not found on top of each other. The characteristic scale of this repulsive core is $\sim\theta_*$ (Bardeen *et al.*, in preparation). Beyond this scale, hotspots are strongly clustered as indicated by equation (3.8). Fig. 3(c) shows these correlation functions for a number of thesholds. Hotspots and coldspots do not strongly cluster together.

The fractional variance in the peak number from realization to realization over a grid of area Ω_{patch} is related to the correlation function by

$$\langle(\Delta N_{pk})^2\rangle/\langle N_{pk}\rangle^2=\langle N_{pk}\rangle^{-1}+\int\int C_{pk,pk}(\hat{q}-\hat{q}')\frac{d\Omega_{\hat{q}}}{\Omega_{patch}}\frac{d\Omega_{\hat{q}'}}{\Omega_{patch}}, \tag{3.9}$$

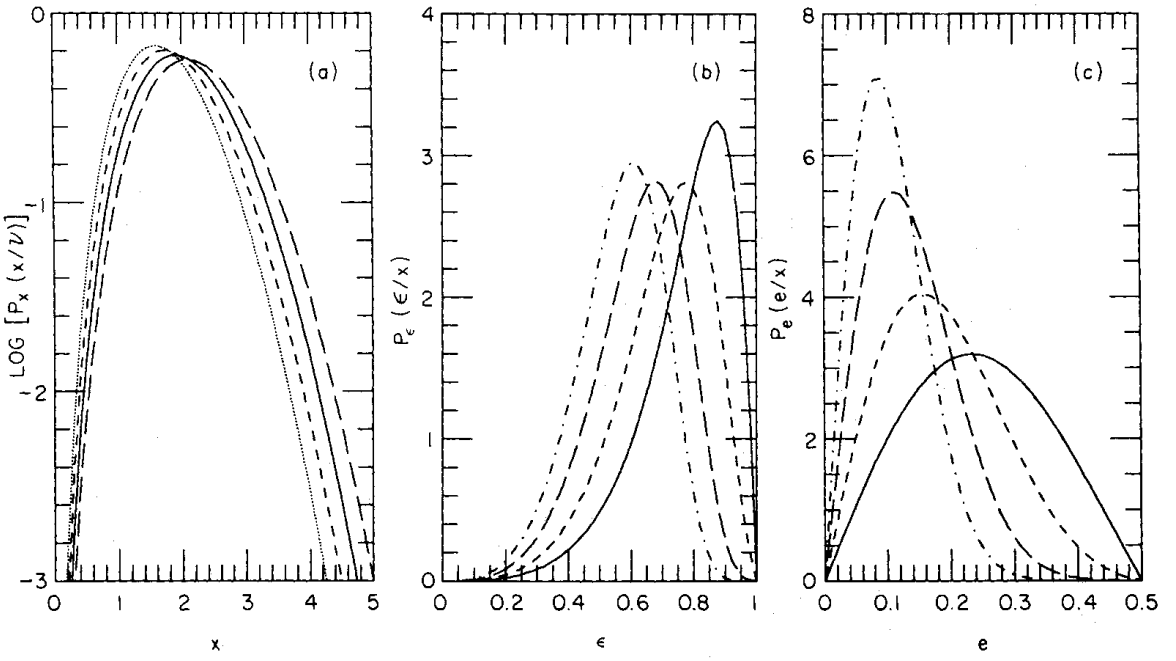

Figure 2. (a) The conditional probability of the curvature parameter $x=|\nabla^2 F/\sigma_2|$ given the height $\nu=0$ (dot), 1 (short dash), 2 (solid), 3 (long dash) of the maximum (or minimum) is plotted for $\gamma=0.347$, the value appropriate to the $h=0.75$ adiabatic CDM model. The eccentricity (b) and ellipticity (c) distributions for $x=1$ (solid), 2 (short dash), 3 (long dash) and 4 (dot-dash) are independent of the spectral parameters and ν. Integration over x gives the ε and e distributions for specified values of the peak height ν [equation (A2.6), Appendix 2].

where the $\langle N_{\rm pk}\rangle \equiv n_{\rm pk}(\nu_{\rm t})\,\Omega_{\rm patch}$ term gives the Poisson fluctuations and the continuous integral reflects the excess variance over Poisson in the map due to clustering. The rms fluctuations are therefore larger for high peaks, by a factor of $\sim A^{1/2}$.

4 Computations of angular correlations and power spectra

The general techniques for calculating small-angle anisotropies in the CMB radiation have been described in a number of papers (e.g. Peebles & Yu 1970; Doroshkevich, Zel'dovich & Sunyaev 1978, hereafter DZS; Wilson & Silk 1981; Bond & Efstathiou 1984, hereafter BE). In this paper, we require computations of $C(\theta)$ which are accurate over the entire angular range. In Section 4.1 we show how this may be accomplished for $\Omega=1$ models. The restriction to flat models considerably simplifies the determination of large-angle anisotropies since then the mode functions for the perturbations are simple plane waves. Furthermore, $\Omega=1$ is a natural outcome of inflationary models in which well-defined predictions of the initial fluctuations can be made. Thus, the techniques developed here allow us to make highly specific predictions of the CMB anisotropies in inflationary models, particularly those in which CDM dominates the present density. In contrast, the initial perturbations in $\Omega<1$ models are *ad hoc*; it is not even clear how to parameterize the fluctuations in a simple way, since the models contain a characteristic scale, that of the curvature. (See Wilson 1982, 1983 for a discussion of anisotropies in open cosmological models.)

In Section 4.1 we first present our methods for exactly computing $C(\theta)$ and then discuss approximate methods. We present results for $C(\theta)$ for several adiabatic CDM models and for one isocurvature model. The spectral parameters required for the statistical formulae in Section 3 are given in Section 4.2. In Section 4.3, we describe methods for evaluating the power spectrum C_l. Accurate fitting formulae for the correlation functions are presented in Section 4.4. In the

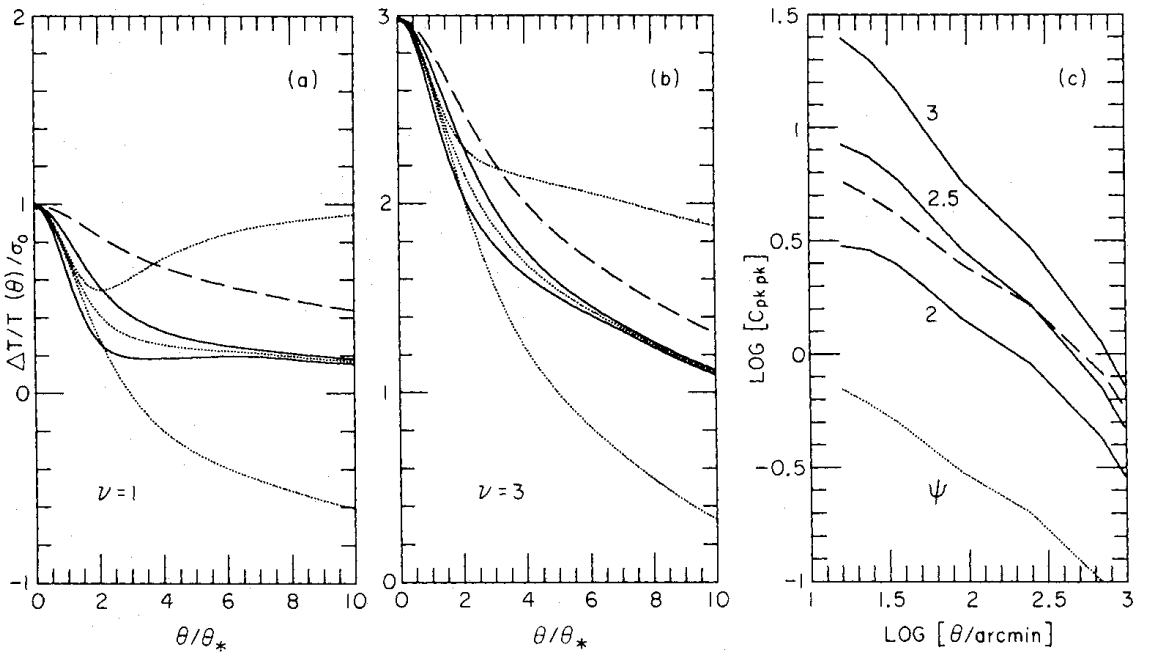

Figure 3. Typical profiles for (a) $\nu=1$ and (b) $\nu=3$ peaks. Average values for the ellipticity, e, (0.2 and 0.15) and the curvature parameter, x, (0.189 and 0.224) have been chosen. The spectral parameters $\gamma=0.347$, $\theta_*=4.59$ arcmin and the profile for field points of height ν, $\nu\psi$ (dash), are those for the unsmoothed $h=0.75$ adiabatic CDM model. This profile is not as steep as the profile about a peak. Comparison of the profiles along the principal 1 and 2 axes (solid) demonstrates that $\nu=1$ peaks are quite elongated and $\nu=3$ peaks are moderately aspherical. The angle-averaged profile, which is the cross-correlation function $C_{\text{pk},\Delta}(\theta)/\sigma_0$, and the $\pm1\sigma$ curves (dashed curves) are also shown. The latter illustrate that peaks are coherent only out to a few θ_* even for $\nu=3$. (c) Shows the correlation functions for peaks (solid) of height in excess of the thresholds $\nu_t=2$, 2.5, 3 computed using the approximations of Appendix 4 [equation (A4.10)]. Again $\gamma=0.347$ was chosen. The normalized correlation function ψ is shown for comparison (dot). For $\nu=3$, $C_{\text{pk,pk}}$ is compared with the extension to small θ of the asymptotic form of the peak correlation function (dash), $\langle\tilde{\nu}\rangle^2\psi(\theta)$ [equation (A4.15)].

following, we do not explicitly include the ensemble average symbol $\langle-\rangle$ where the averaging is clear, as in expressions for $C(\theta)$, C_l and the spectral parameters σ_p of equation (2.15).

4.1 COMPUTATIONS OF THE CORRELATION FUNCTION

Our method for evolving the radiation field through recombination has been discussed in BE. Briefly, we decompose the perturbations into plane waves, solve the Boltzmann transport equations for the total radiation intensity fluctuations Δ_T and linear polarization fluctuations Δ_P by expanding both in Legendre polynomials,

$$\Delta_T(\mathbf{k},\hat{q},\tau)=\sum_l (2l+1)\,\Delta_{Tl}(k,\tau)\,P_l(\mu), \qquad \mu\equiv\hat{k}\cdot\hat{q}, \tag{4.1}$$

and evolving the hierarchy of coupled equations for the Δ_{Tl} and Δ_{Pl}. These equations are coupled to evolution equations for the baryon density and velocity, the CDM density, the Boltzmann equation for three massless neutrino flavours and the perturbed Einstein equations in the synchronous gauge for the scalar metric fluctuations h and h_{33}. The equations are given in BE, Efstathiou & Bond (1986, hereafter EB), and Bond & Szalay (1983) and will not be repeated here. We assume the standard recombination physics as described by Peebles (1968); reionization is discussed in a separate paper.

The temperature autocorrelation function is given by

$$C(\theta, \tau_0) \equiv \frac{V_x}{32\pi^2} \int_0^\infty \sum_{l\geq 2} (2l+1) \mid \Delta_{Tl}(k, \tau_0) \mid^2 P_l(\cos\theta)\, k^2\, dk, \tag{4.2}$$

where V_x is a box-normalization volume for the plane waves. An analogous expression holds for the polarization correlation function $C_P(\theta)$. The relationship between C_P and observations of polarization is discussed in Appendix 5. In practice, we evolve the hierarchy of equations for $\Delta_{Tl}(k, \tau)$ until an epoch τ_s when recombination is complete and the optical depth to the observer is negligible. After τ_s, the radiation obeys the free-streaming equation

$$\begin{aligned} &\dot{\Delta}_T + i\hat{q}\cdot\mathbf{k}\,\Delta_T = (1-\mu^2)\,\dot{h} + (3\mu^2-1)\,\dot{h}_{33}, \\ &\dot{\Delta}_P + i\hat{q}\cdot\mathbf{k}\,\Delta_P = 0, \end{aligned} \tag{4.3}$$

where the dot denotes differentiation with respect to τ. Let us define auxiliary variables

$$\begin{aligned} &\tilde{\Delta}_{T0} = \Delta_{T0} - 2\ddot{h}/k^2, \\ &\tilde{\Delta}_{T1} = \Delta_{T1} + \frac{2i}{3k}\dot{h}, \\ &\tilde{\Delta}_{Tl} = \Delta_{Tl}, \qquad l\geq 2. \end{aligned} \tag{4.4}$$

When the approximations $h \propto \tau^2$ and $\dot{h}_{33} \approx \dot{h}$ apply, as occurs in adiabatic models once after the universe becomes matter dominated, then $\tilde{\Delta}_{Tl}$ at τ_0 is related to $\tilde{\Delta}_{Tl}(k, \tau_s)$ by

$$\tilde{\Delta}_{Tl}(k, \tau_0) = \sum_{l'} \sum_{m=0}^{\min(l, l')} \tilde{\Delta}_{Tl'}(k, \tau_s)(2l'+1) \frac{c_{l, l', m}}{i^{l+l'-2m}} j_{l+l'-2m}(k\Delta\tau), \tag{4.5}$$

where

$$\Delta\tau = \tau_0 - \tau_s,$$

and

$$\begin{aligned} &c_{l, l', m} = \frac{\alpha_{l'-m}\alpha_m\alpha_{l-m}}{\alpha_{l+l'-m}} \frac{2l+2l'-4m+1}{2l+2l'-2m+1}, \\ &\alpha_n = \frac{(2n-1)!!}{n!}. \end{aligned}$$

An equivalent expression holds for $\Delta_{Pl}(k, \tau_0)$. It is computationally much faster to evaluate this series than to evolve the coupled free-streaming equations for the Δ_ls.

Our procedure for the adiabatic case is as follows: we evolve the full set of integro-differential equations as in BE to a redshift of about 300. Beyond this time the series expansion, equation (4.5), accurately describes the subsequent evolution of the radiation. We have checked that the solutions derived in this way are highly accurate using a number of tests. First, equations (4.3) require a conservation condition,

$$\sum_{l=0}^{\infty} (2l+1) \mid \tilde{\Delta}_{Tl}(k, \tau_0) \mid^2 = \sum_{l=0}^{\infty} (2l+1) \mid \tilde{\Delta}_{Tl}(k, \tau_s) \mid^2. \tag{4.6}$$

Secondly, as the radiation free-streams, $\mid \tilde{\Delta}_T(k, \mu, \tau) \mid$ retains the same functional form. Thirdly, we have compared the series solution of equation (4.5) with the direct evolution of equation (4.3) to the present. These tests show that our final results are accurate to within a few per cent. The

Table 1. Parameters for scale-invariant CDM models.

Mode	Ad	Ad	Ad	Ad	Is
h	1.0	0.75	0.50	0.50	0.75
Ω_B	0.03	0.03	0.03	0.10	0.03
$b\sigma_0(\times 10^5)$	1.52	1.80	2.79	3.54	12.2
γ	0.322	0.347	0.391	0.342	0.158
θ_*	4.32	4.59	5.17	3.79	8.44
θ_c	12.59	12.84	12.76	10.94	53.2
$b\sigma_{p0}(\times 10^6)$	0.711	1.05	1.84	1.98	2.44
γ_p	0.680	0.693	0.693	0.667	0.524
θ_{*p}	3.26	3.66	4.23	2.90	5.36
θ_{cp}	4.79	5.28	6.11	4.35	10.2
$A(\times 10^{10})$	1.84	1.96	5.87	9.90	95.44
$\varkappa$	0.326	0.216	0.172	0.0920	0.0613
$a_2(\times 10^6)$	4.46	5.70	8.75	9.93	64.9
θ_1	167.2	57.05	61.91	44.10	311.1
θ_2	9.719	7.011	6.725	4.428	15.23
θ_3	24.01	9.380	8.694	5.688	26.42
θ_4	172.1	33.51	148.7	116.4	521.0
$\varkappa_p$	0.0184	0.0192	0.0131	0.0120	0.206
θ_{p1}	7.547	8.314	9.495	6.744	34.34
θ_{p2}	2.090	2.361	2.376	1.639	7.234
θ_{p3}	2.511	2.823	2.839	1.976	9.248

Notes

Ad denotes adiabatic mode; Is denotes isocurvature mode. The quoted values of γ and θ_* were derived by applying a smoothing of $\theta_s=1$ arcmin. $\theta_s=0$ for the other spectral parameters listed. All angles are quoted in arcmin.

sum in equation (4.5) must extend to $l>k\tau_0$. Thus, for high wavenumbers, large values of l are required. We use Miller's method (Abramowitz & Stegun 1970) for evaluating the spherical Bessel functions.

The evolution of isocurvature fluctuations has been described in detail by EB. In this case, equation (4.5) cannot be used until $h\propto\tau^2$, which occurs in the matter-dominated regime only for wavelengths much smaller than the horizon. For long wavelengths we evolved equations (4.3) until this condition was satisfied or until τ_0 was reached.

We have used the above procedures to compute correlation functions for several $\Omega=1$ adiabatic CDM models. The parameters for these models are listed in Table 1. We also present results for one isocurvature CDM model with $h=0.75$ and $\Omega_B=0.03$. The scale-invariant isocurvature model faces a number of difficulties especially when compared with large angle anisotropy limits (EB) and is included primarily to contrast with the $h=0.75$, $\Omega_B=0.03$ adiabatic case. These two models are compared in detail in this and the next section.

In Fig. 4(a) and (c), we plot $k^3W_T^2(\theta, k)$, the integrand of equation (4.2), where

$$W_T^2(\theta,k)\equiv\sum_{l\geq 2}(2l+1)\,|\,\Delta_{Tl}(k,\tau_0)\,|^2\,P_l(\cos\theta), \tag{4.7}$$

for several values of θ. This illustrates the contribution to $C(\theta)$ from each decade of wavenumber for scale-invariant initial conditions. In the adiabatic model, the fundamental role played by the horizon at recombination is evident. For longer wavelengths, only the Sachs–Wolfe effect due to anisotropies in the gravitational potential fluctuations contributes. The flat part is equal to $\ddot{h}^2(k,\tau_0)/k$ which reflects the scale-independence of the initial potential fluctuations. The two large peaks arise from anisotropies generated by Thomson scattering off the moving electrons on

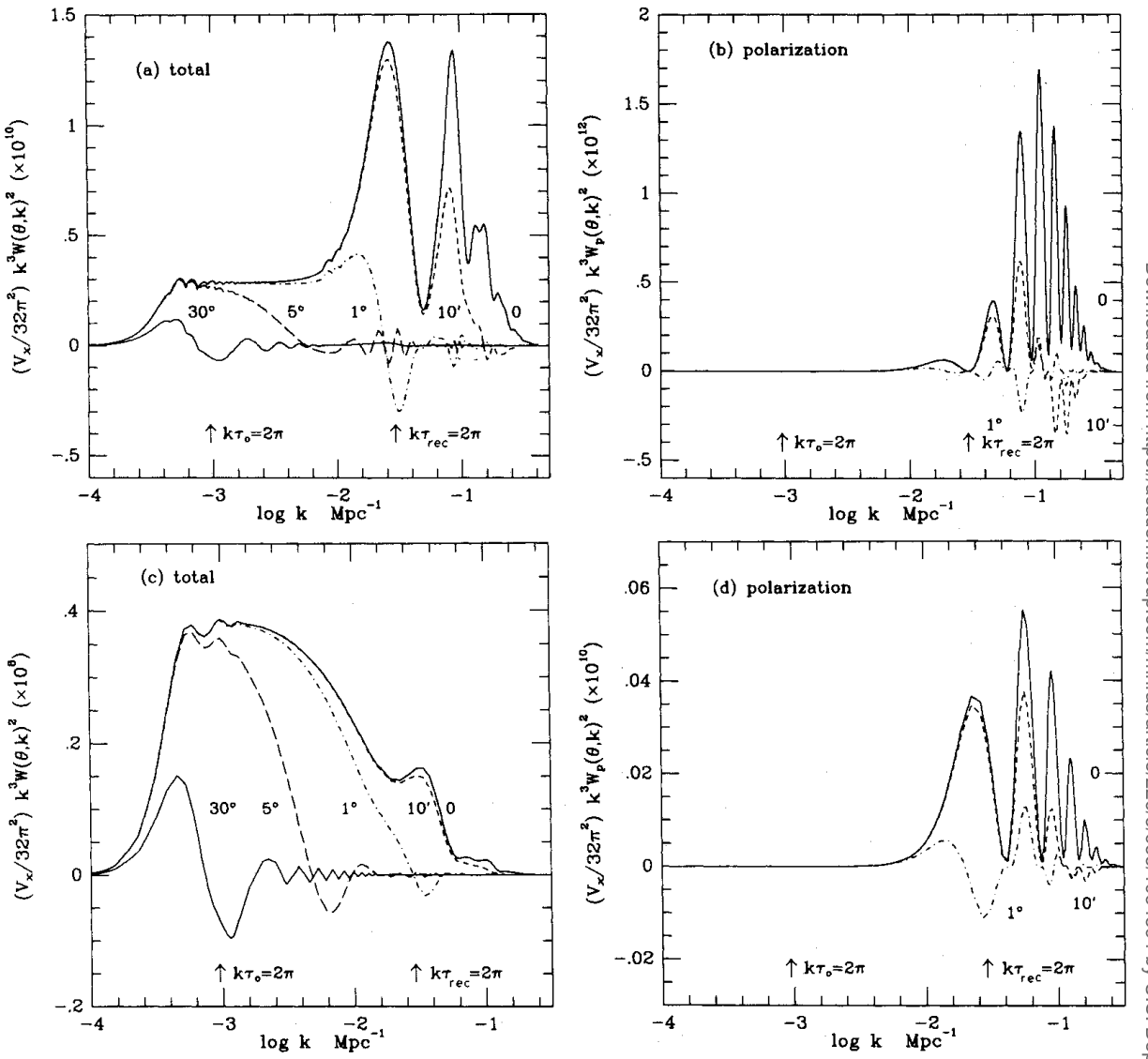

Figure 4. Integrands of the radiation autocorrelation function $k^3W_T^2(\theta, k)$ plotted against $\log k$ for various θ. (a, b) Show the integrands for the total and polarization correlation functions, respectively for a scale-invariant adiabatic CDM model with $\Omega=1$, $\Omega_B=0.03$, $h=0.75$. (c, d) Show the equivalent plots for a scale-invariant isocurvature CDM model with identical cosmological parameters. The area under each curve gives $C(\theta)$ thus it is easy to assess how fluctuations on various scales would contribute to experiments probing any particular angle. These curves have been normalized according to the prescription given in Section 4.2 with the biasing parameter $b=1$.

scales smaller than the horizon at recombination, τ_{rec}. On scales smaller than the width of the last scattering surface, these anisotropies are cancelled by contributions from oppositely directed velocity flows across the wave. Fig. 4(b) and (d) show analogous plots for the polarization $[k^3W_P^2(\theta, k)]$. The power in the polarization correlation function comes almost entirely from scales smaller than τ_{rec}, generated as a result of the polarization dependence of the Thomson scattering cross-section.

In the isocurvature models, the total correlation function $C(\theta)$ has much more power on large scales than in the adiabatic model due to the *isocurvature effect* described by EB: while wavelengths are larger than the horizon, the isocurvature initial conditions require that the total energy density remain close to zero. The fluctuations in the entropy per CDM particle, which are also set by the initial conditions, must remain constant. As the universe passes from radiation to

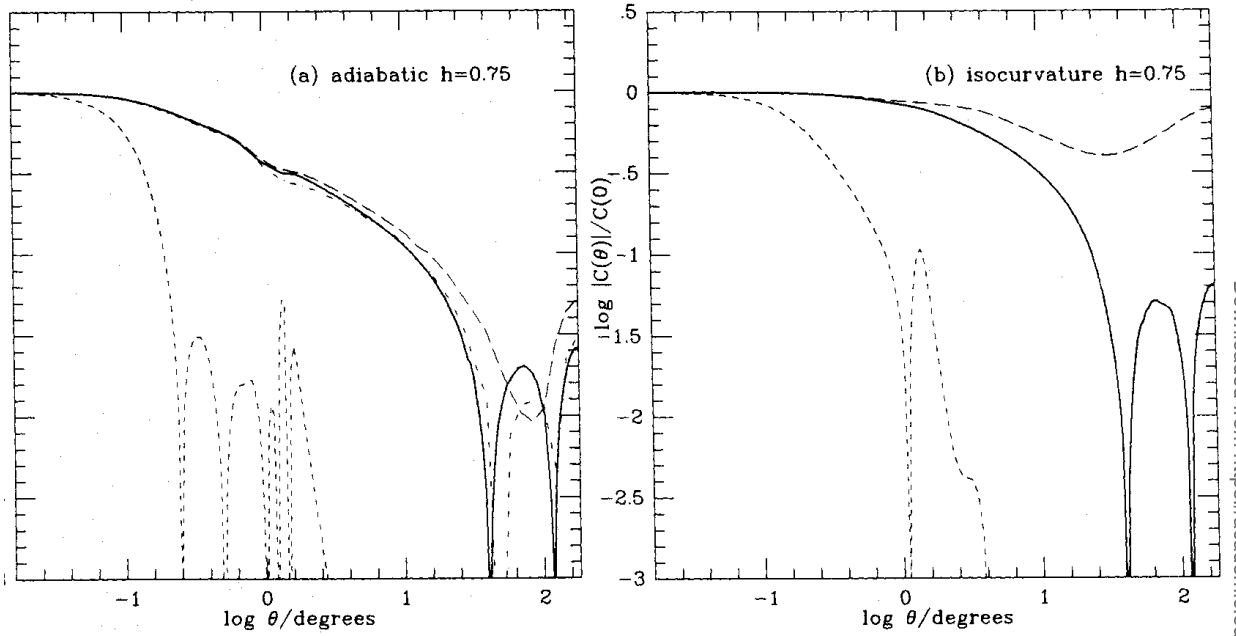

Figure 5. The solid lines show the autocorrelation functions of the total intensity fluctuations for the two scale-invariant CDM models shown in Fig. 4. The dotted lines show the polarization correlation function $C_P(\theta)$. We have plotted the logarithm of the absolute value of $C(\theta)$ with the understanding that a zero-crossing occurs whenever a curve hits the x-axis in these plots. The long-dashed lines show the approximation to $C(\theta)$ given by equation (4.11) and the dot–dashed line shows the approximation of equation (4.14). For the isocurvature model shown in (b) these two approximations give nearly identical results.

matter domination these two constraints necessitate a transfer of the fluctuation from the CDM to the photons and baryons, building up the radiation perturbation amplitude. The peak in the $C(\theta)$ power is related to the initial scale-invariant power in the CDM perturbations $|\delta_{Xi}|^2 \propto k^{-3}$ by

$$k^3 W_T^2(\theta=0,k)=(4/3+\gamma)^2 k^3 |\delta_{Xi}|^2, \qquad \gamma=0.266. \tag{4.8}$$

The part involving γ represents the usual Sachs–Wolfe effect, while the rest is due to the isocurvature effect. Deviations from flatness in Fig. 4(c) arise since the transfer of the fluctuation amplitude from CDM to radiation is arrested once the waves come within the horizon and the CDM perturbations begin to grow. For waves that enter the horizon before τ_{rec}, the physical effects, including the generation of the polarization amplitude, are similar to those in the adiabatic case discussed above.

The correlation functions $C(\theta)$ and $C_P(\theta)$ for these two models are shown in Fig. 5 for scale-invariant initial conditions. The large-angle form of $C(\theta)$ is well described by

$$C(\theta) \approx \frac{3a_2^2}{2\pi}\left[\ln\left(\frac{2}{1-\cos\theta}\right)-1-\tfrac{3}{2}\cos\theta\right]. \tag{4.9}$$

This follows from the Sachs-Wolfe contribution $\Delta_{Tl}=(-2\ddot{h}/k^2)\, j_l(k\tau_0)/i^l$ in the adiabatic case and from an identical analysis using equation (4.8) in the isocurvature case.

Previous numerical calculations of $C(\theta)$ have been based on small-angle formulae (e.g. DZS; Wilson & Silk 1981; BE; Vittorio & Silk 1984). These approximations can yield poor estimates for the shape of $C(\theta)$ and for the value of $C(0)$ in cases when substantial power exists on large scales (as with scale-invariant perturbations), although the difference $C(0)-C(\theta)$ (which is all that is required for comparison with small-angle experiments) is computed accurately. For example, the fits to $C(\theta)$ derived for CDM models in BE using the small-angle approximation of Wilson & Silk

(1981) are inappropriate for the applications described in this paper and could give a false impression of the characteristics of the radiation field. Here we derive formulae which extend the small-angle approximations of DZS [equation (4.11)] and of Wilson & Silk [equation (4.14)] by including the Sachs–Wolfe and isocurvature effects. For $\theta \ll 1$

$$\tilde{\Delta}_T(k, \hat{k}\cdot\hat{q}, \tau_0)\,\tilde{\Delta}_T^*(k, \hat{k}\cdot\hat{q}', \tau_0) \approx |\,\tilde{\Delta}_T(k, \hat{k}\cdot\hat{q}, \tau_s)\,|^2 \exp[i\mathbf{k}\cdot(\hat{q}-\hat{q}')\,\Delta\tau]. \tag{4.10}$$

The rigorous conservation theorem equation (4.6) leads to the following expression once monopole and dipole terms have been subtracted:

$$C(\theta) \approx \frac{V_x}{32\pi^2}\int_0^\infty k^2\,dk\left\{\frac{1}{2}\int_{-1}^{1} d\mu\;|\;\tilde{\Delta}_T(k, \mu, \tau_s)\;|^2\;J_0[k\tau_0\varpi(1-\mu^2)^{1/2}]\right.$$

$$\left. -|\,\tilde{\Delta}_{T0}(k, \tau_0)\,|^2 - 3\cos\theta\,|\,\tilde{\Delta}_{T1}(k, \tau_0)\,|^2\right\}, \qquad \tau_0 \gg \tau_s, \tag{4.11}$$

where

$$\tilde{\Delta}_{T0}(k, \tau_0) = -\frac{2\ddot{h}(\tau_s)}{k^2} j_0(k\Delta\tau) + \frac{2\dot{h}(\tau_s)}{k} j_1(k\Delta\tau) + \sum_{l=0}^{\infty}(2l+1)\;\Delta_{Tl}(k, \tau_s)\,j_l(k\Delta\tau)/i^l,$$

$$\tilde{\Delta}_{T1}(k, \tau_0)/i = \frac{2\ddot{h}(\tau_s)}{k^2} j_1(k\Delta\tau) - \frac{2\dot{h}(\tau_s)}{3k}[2j_2(k\Delta\tau) - j_0(k\Delta\tau)]$$

$$-\sum_{l=0}^{\infty}\frac{\Delta_{Tl}(k, \tau_s)}{i^l}[(l+1)\,j_{l+1}(k\Delta\tau) - l j_l(k\Delta\tau)]. \tag{4.12}$$

In Fig. 5, this approximation is shown as the long-dashed lines. It works quite well out to $\sim 10°$ in the adiabatic case, but less well for the isocurvature model.

Another approximation, which is more accurate for the adiabatic models, may be derived as follows. The solution to the free streaming equation gives

$$\tilde{\Delta}_{Tl}(k, \tau_0) = \frac{1}{2}\int_{-1}^{1} d\mu\,\tilde{\Delta}_T(k, \mu, \tau_s)\,\exp(-ik\mu\Delta\tau)\,P_l(\mu).$$

For $l \gg 1$, the function $P_l(\mu)$ has width $\sim l^{-1}$, whilst $\tilde{\Delta}_T(k, \mu, \tau_s)$ is a single peaked function of width $\sim (k\tau_{rec})^{-1}$ for $k\tau_{rec} > 1$. Thus, for $l > k\tau_{rec}$, $\tilde{\Delta}_{Tl}(k, \tau_0)$ is approximately the convolution of the Fourier transforms of $\tilde{\Delta}_T(k, \mu, \tau_s)$ and P_l, the former being a narrow function of $k\Delta\tau$ and the latter broad [$\propto j_l(k\tau_0)$]. We therefore lose little accuracy in writing

$$|\,\tilde{\Delta}_{Tl}(k, \tau_0)\,|^2 \approx W_T^2(0, k)\,j_l^2(k\tau_0), \qquad l \gg k\tau_{rec}, \qquad k\tau_0 \gg 1. \tag{4.13}$$

The constant multiplier $W_T^2(0, k)$, evaluated at τ_s, is fixed by the conservation theorem equation (4.6). Our comparisons with the exact solution, equation (4.5), show that at fixed k equation (4.13) provides an accurate description apart from a slow variation of the phase of j_l with l. Equation (4.13) is the basis of the small-angle approximation used by Wilson & Silk and BE. Substituting in equation (4.2) and subtracting monopole and dipole terms as in equation (4.11) gives

$$C(\theta) \approx \frac{V_x}{32\pi^2}\int_0^\infty k^2\,dk[W_T^2(0, k)\,j_0(k\tau\varpi) - |\,\tilde{\Delta}_{T0}(k, \tau_0)\,|^2 - 3\cos\theta\,|\,\tilde{\Delta}_{T1}(k, \tau_0)\,|^2]. \tag{4.14}$$

In Fig. 5(a), this approximation is shown by the dot–dashed line and agrees extremely well with the exact solution out to the first zero of $C(\theta)$. For the isocurvature model, equation (4.14) gives almost identical answers to equation (4.11). The poorer performance of both approximations in

Fig. 5(b) arises because long wavelengths ($k\tau_0 \sim 1$) make a proportionately larger contribution to $C(\theta)$ than for the adiabatic model shown in Fig. 5(a) (see Fig. 4).

4.2 SPECTRAL PARAMETERS

The formulae in Section 3 require the calculation of the spectral parameters σ_0, σ_1 and σ_2 which are given by the following exact expressions:

$$\sigma_0^2 = \frac{V_x}{32\pi^2}\int_0^\infty k^2\,dk \sum_{l=2}^{\infty}(2l+1)\,|\,\mathscr{F}_l\,|^2|\,\Delta_{Tl}|^2,$$

$$\sigma_1^2 = \frac{V_x}{32\pi^2}\int_0^\infty k^2\,dk \sum_{l=2}^{\infty}(2l+1)\,l(l+1)\,|\,\mathscr{F}_l\,|^2|\,\Delta_{Tl}|^2,$$

$$\sigma_2^2 = \frac{V_x}{32\pi^2}\int_0^\infty k^2\,dk \sum_{l=2}^{\infty}(2l+1)\,(l+2)(l+1)\,l(l-1)\,|\,\mathscr{F}_l\,|^2|\,\Delta_{Tl}|^2. \tag{4.15}$$

In the absence of beam-smearing, σ_1 and σ_2 have substantial contributions from high wavenumbers where application of equation (4.2) is impractical ($k\tau_0 > 5000$). To overcome this limitation, we can use equations (4.15) with the upper limit of the k-integral set to k_m and adding the following integrals derived from the derivatives of the small-angle approximation, equation (4.12):

$$\Delta\sigma_0^2 = \frac{V_x}{32\pi^2}\int_{k_m}^\infty k^2\,dk\left[\frac{1}{2}\int_{-1}^{1}d\mu\,|\,\tilde{\Delta}_T(k,\mu,\tau_s)\,|^2 - |\,\Delta_{T0}(k,\tau_0)\,|^2 - 3\,|\,\Delta_{T1}(k,\tau_0)\,|^2\right],$$

$$\Delta\sigma_1^2 = \frac{V_x}{32\pi^2}\int_{k_m}^\infty k^2\,dk\left[\frac{1}{2}\int_{-1}^{1}d\mu\,|\,\tilde{\Delta}_T(k,\mu,\tau_s)\,|^2(1-\mu^2)(k\tau_0)^2 - \tfrac{3}{4}\,|\,\Delta_{T1}(k,\tau_0)\,|^2\right],$$

$$\Delta\sigma_2^2 = \frac{V_x}{32\pi^2}\int_{k_m}^\infty k^2\,dk\left[\frac{1}{2}\int_{-1}^{1}d\mu\,|\,\tilde{\Delta}_T(k,\mu,\tau_s)\,|^2(1-\mu^2)^2(k\tau_0)^4\right]. \tag{4.16}$$

To include Gaussian smoothing in equation (4.16) $|\,\tilde{\Delta}_T(k,\mu,\tau_s)\,|^2$ should be multiplied by $\exp[-(1-\mu^2)(k\tau_0\theta_s)^2]$. Even with $k_m = 0$, the results from equation (4.16) are extremely accurate. For scale-invariant initial conditions σ_2 diverges logarithmically at high k. Strictly speaking, the predicted anisotropy field is a non-differentiable random field since $C^{(iv)}(0)$ does not exist. The physical origin of this divergence is from a small-scale Sachs–Wolfe term which leads to a contribution to the rms temperature fluctuations of

$$W_T(0,k) \approx \frac{9}{2}\frac{\ddot{h}}{k^2}\left(\frac{\varrho_B}{\varrho\gamma}\right)_{\tau_{rec}}.$$

However, this is unlikely to be of interest in any conceivable experiment since even for small beam widths ($\theta_s < 1$ arcmin) the net contribution of this effect to $C^{(iv)}(0)$ is negligible.

To normalize σ_0 we have matched values of

$$J_{3\varrho}(x_0) = \int_0^{x_0}\xi_\varrho(x)\,x^2\,dx$$

computed using the density fluctuation spectra at τ_0 for our CDM models to the value $J_{3g}(x_0)$ determined from the galaxy autocorrelation function ξ_g measured in the CfA survey for $x_0 = 10\,h^{-1}$ Mpc (see BE for details). This normalization is only appropriate if galaxies trace the

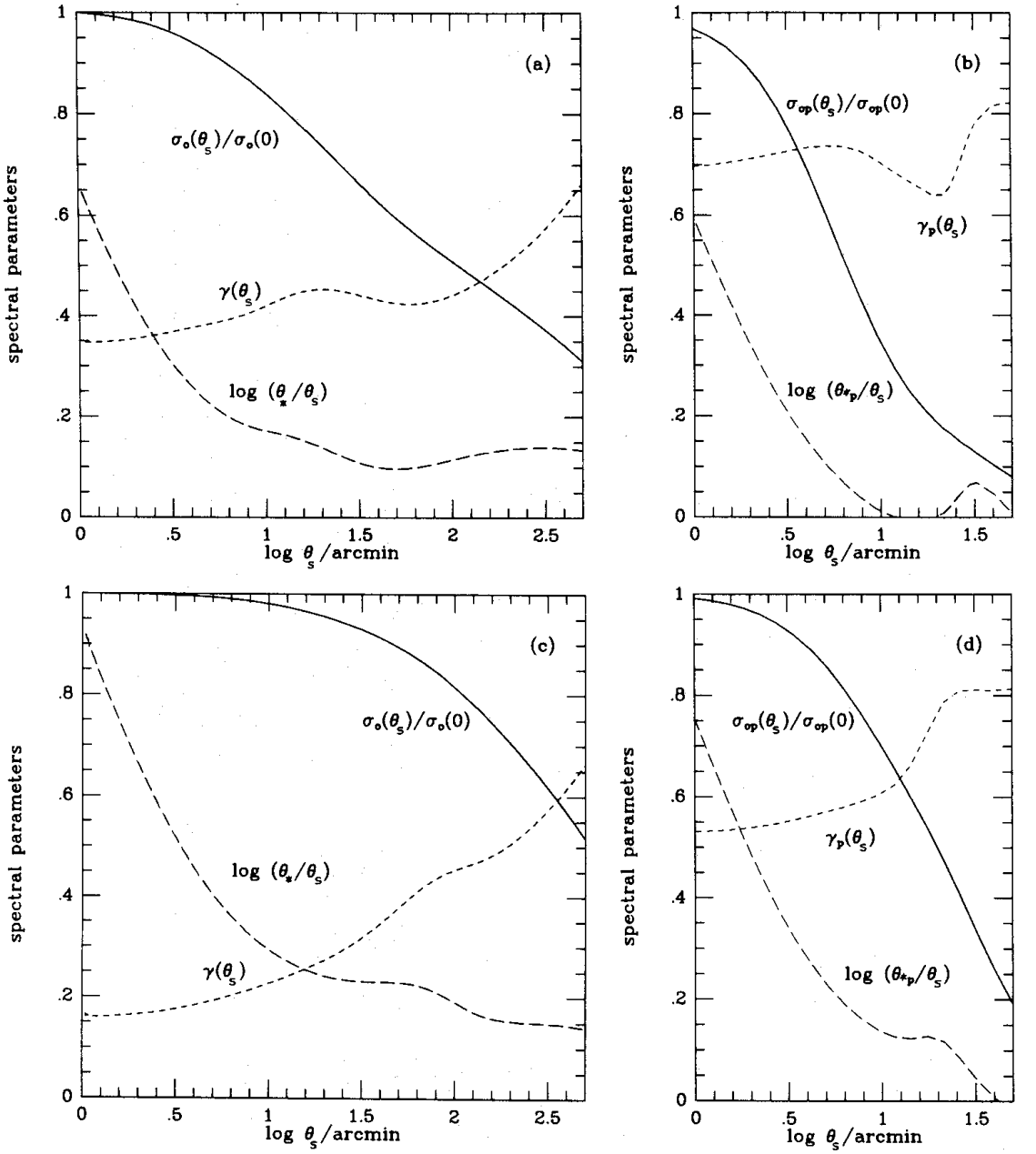

Figure 6. The spectral parameters σ_0, γ and θ_* as a function of smoothing angle θ_s. (a, b) Show these parameters for the total and polarization fluctuations respectively for the $h=0.75$ scale-invariant adiabatic CDM model. (c, d) Show equivalent plots for the $h=0.75$ scale-invariant isocurvature model.

mass distribution. In the $\Omega=1$ CDM model galaxies are assumed to be more clustered than the mass distribution so that dynamical estimates of the value of Ω may be reconciled with the underlying assumption that $\Omega=1$ (e.g. Davis *et al.* 1985; BBKS). Our models are consistent only if we include this effect. We therefore quote values for $b\sigma_0$, where $b^2 \equiv J_{3g}(x_0)/J_{3\varrho}(x_0)$, with the understanding that appropriate values for b lie within the range 1.5–2.5 (see BBKS). Values for $b\sigma_0$, θ_c, γ and θ_* together with the analogous quantities for polarization fluctuations are listed in Table 1 for each of our models. In Fig. 6, we show $b\sigma_0$, γ and θ_*/θ_s as a function of the smoothing angle θ_s for our two $h=0.75$ models. It is straightforward to evaluate these spectral parameters for the total intensity fluctuations using the analytic fits to $C(\theta)$ provided in Table 1 (see Section 4.4. below) together with equation (2.12) and its derivatives evaluated at $\theta=0$. The spectral

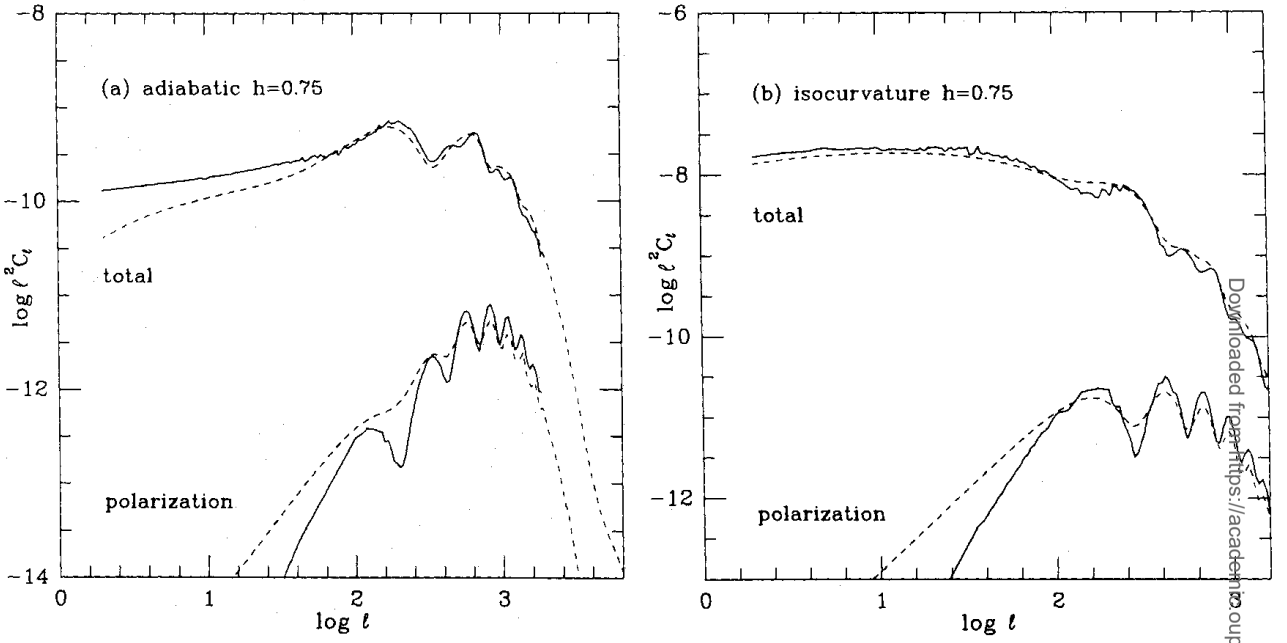

Figure 7. Power spectra for the two $h=0.75$ scale-invariant CDM models. The solid lines show results from equation (4.17) and the dotted lines show approximate results derived from equation (4.19).

parameters characterizing the polarization fluctuations must be calculated either by using equations (4.15) and (4.16) or by interpolating the numerical computations of $C_P(\theta)$ together with equation (2.12) since it is not possible to provide simple analytic formulae for the complex behaviour shown in Fig. 5 (but see Section 4.4 for analytic fits which are accurate at $\theta<10$ arcmin).

4.3 EVALUATION OF POWER SPECTRA

The sections above have described how to obtain the various correlation properties required to specify the statistical characteristics of the radiation field. To simulate the temperature fluctuations, as we will do in Section 5, we require the power spectra of our models. Equations (2.2) and (4.2) give

$$C_l=\frac{V_x}{8\pi}\int_0^\infty k^2\,dk\,|\,\Delta_{Tl}(k,\tau_0)\,|^2. \tag{4.17}$$

For low values of $l(<40)$, where only the Sachs–Wolfe or isocurvature effects are important, equation (4.17) yields

$$C_l=(a_2)^2\frac{\Gamma[l+(n-1)/2]\;\Gamma[(9-n)/2]}{\Gamma[l+(5-n)/2]\;\Gamma[(3+n)/2)]}, \qquad n<3, \qquad l\geq 2, \tag{4.18}$$

where n is the spectral index ($|\,\delta_X(k,\tau_0)\,|^2\propto k^n$) on comoving scales much larger than the horizon at the epoch of equal density of matter and radiation. For scale-invariant fluctuations ($n=1$) $C_l\propto l^{-2}$, corresponding to scale-invariance in two dimensions.

For $l\gg 1$, each Δ_{Tl} is a highly oscillatory function of k and is approximately given by equation (4.13). At large l

$$\langle j_l^2(z)\rangle\approx[2z(z^2-l^2)^{1/2}]^{-1}, \qquad z>l,$$
$$\approx 0, \qquad z<l.$$

Thus a useful approximation to C_l is

$$C_l \approx \frac{V_x}{8\pi} \int_{l/\tau_0}^{\infty} \frac{k^2\,dk}{2k\tau_0[(k\tau_0)^2 - l^2]^{1/2}} W_T^2(0,k). \tag{4.19}$$

For $k\tau_{rec} \gg 1$, a 3D plane wave make a significant contribution to the sky fluctuations only when seen in a direction perpendicular to the wavevector. Thus naïvely one might expect

$$l^2 C_l \approx \frac{V_x}{16\pi} k^3 W_T^2(0,k), \qquad k = l/\tau_0,$$

so C_l would be describable in terms of a 'transfer function' $\propto W_T$ (i.e. a linear relation with the primordial fluctuation spectrum, e.g. Kaiser 1984). However this expression is only accurate to factors of order unity because $\tilde{\Delta}_T(k,\mu)$ falls with increasing k at about the same rate as it decreases away from $\mu = 0$.

In Fig. 7 we show C_l evaluated for our two $h = 0.75$ CDM models using equations (4.17) and (4.19). The estimates of C_l from equation (4.15) for $l > 20$ have been averaged in logarithmically spaced intervals to smooth the rapid oscillations in k and hence reduce numerical error. Our results do not depend upon the details of the smoothing method used. As Fig. 7 demonstrates, the approximate expression equation (4.19) is quite accurate for $l > 100$. Evaluation of $S(Q)$ using equation (2.7a), after smoothing over Q to reduce numerical error, gives results in agreement with our determination of C_l as expected from equation (2.8)

4.4 FITTING FORMULAE FOR $C(\theta)$

A three-parameter fitting formula describes our correlation functions to within a few per cent over the entire angular range:

$$C(\theta) = \frac{A \exp[-(\theta/\theta_1)^2]}{[1+(\theta/\theta_2)^2+(\theta/\theta_3)^4]^{\varkappa}} + \frac{3a_2^2}{\pi}\{\tfrac{1}{2}\ln(1+4/\theta_4^2) - \tfrac{1}{2} - \tfrac{1}{8}\ln[1+(\varpi/\theta_4)^8] - \tfrac{3}{4}\cos\theta\},$$

$$\varpi = 2\sin(\theta/2). \tag{4.20}$$

The parameters θ_1, $\varkappa$ and θ_4 were determined by non-linear least-squares minimization to our numerical results with the remaining quantities, θ_2, θ_3 and A constrained to reproduce the values for σ_0, γ and θ_* listed in Table 1. The fitted parameters and the quadrupole amplitude a_2 are listed in Table 1. The form of the second term in equation (4.20) was chosen to give equation (4.9) in the large-angle limit and to have small derivatives at the origin. As a rough estimate of the effects of a high pass filter ($l < 40$), the reader may subtract terms from equation (2.2) using the approximate formula (4.18).

The correlation functions describing the degree of polarization cannot be approximated at all angular scales by a simple formula. However, we have fitted $C_P(\theta)$ for $\theta < 10$ arcmin to

$$C_P(\theta) = \frac{\sigma_{P0} \exp[-(\theta/\theta_{P1})^2]}{[1+(\theta/\theta_{P2})^2+(\theta/\theta_{P3})^4]^{\varkappa_P}}. \tag{4.21}$$

As above θ_{P2} and θ_{P3} are fixed by the values of γ_P and θ_{*P}. The best-fitting parameters are listed in Table 1.

5 Maps of the cosmic background radiation

In this section we will generate 10 degree square realizations of the CMB temperature anisotropies using the power spectra obtained in Section 4.3. These pictures provide a graphic

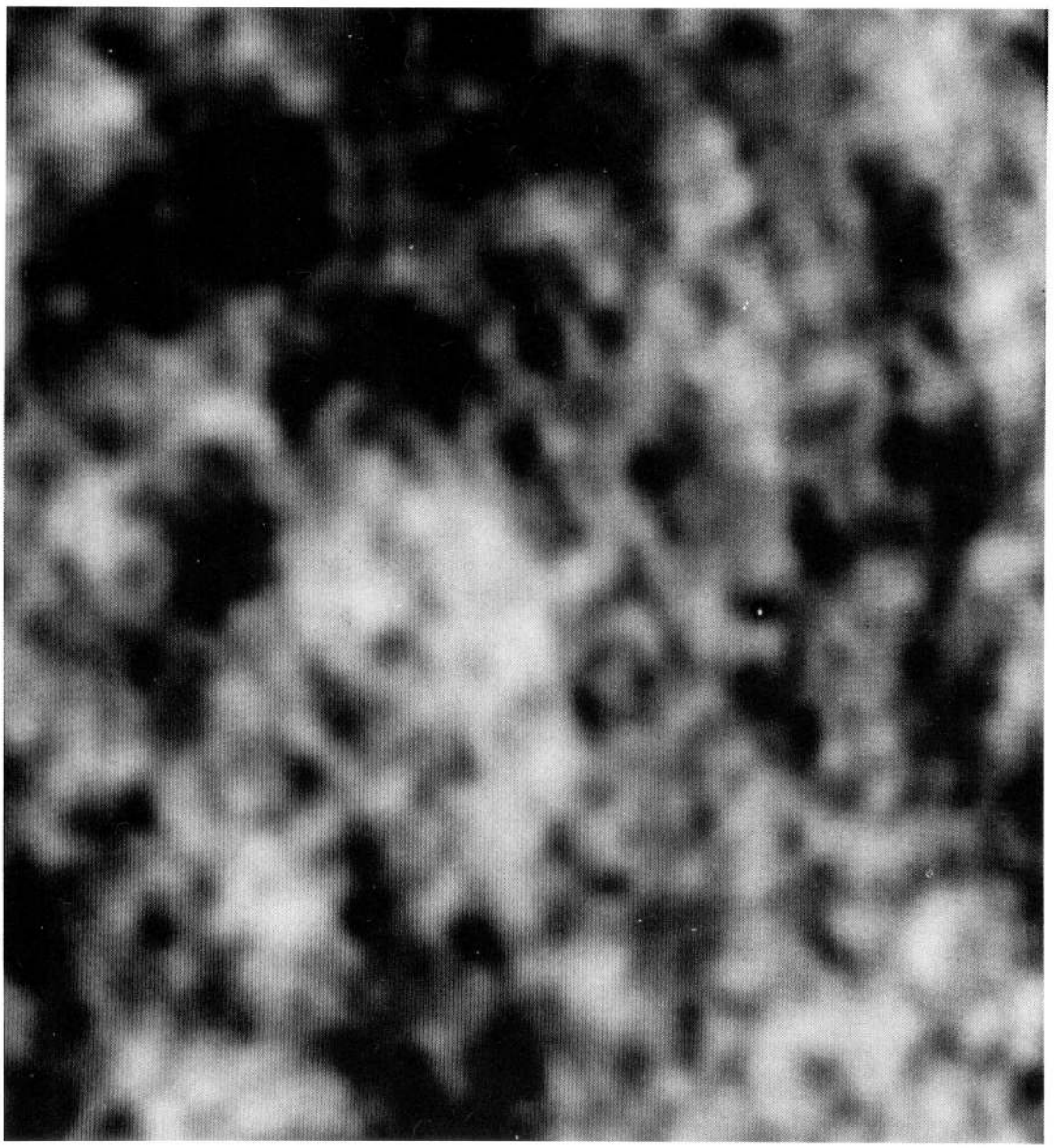

Plate 1. Grey-scale photograph of the total temperature fluctuations in a $10° \times 10°$ patch of sky expected in a scale-invariant adiabatic model with $\Omega = 1$, $\Omega_B = 0.03$, $h = 0.75$.

[*facing page* 674]

1987MNRAS.226..655B

illustration of the texture of the radiation field expected in scale-invariant CDM models, and allow a check of some of the statistical formulae derived in Section 3. Numerically generated maps of this kind would probably be essential to interpret data from experiments in which the effects of high pass filters, asymmetric beam profiles, or l-dependent sensitivity (in interferometric experiments) might have to be taken into account.

Given the spectra C_l shown in Fig. 7, small-angle maps of the radiation fluctuations may be generated by evaluating the Fourier series.

$$\Delta T/T = \sum_{n_x, n_y} D(\mathbf{n}) \exp\left[i \frac{2\pi}{L} \mathbf{n}\cdot\boldsymbol{\theta} \right],$$

where L denotes the size of the simulated region. A Euclidean map with periodic boundary conditions can thus be generated by evaluating a Fast Fourier Transform after selecting the amplitude of $D(\mathbf{n})$ from a Gaussian distribution with zero mean and variance

$$\langle |D(\mathbf{n})|^2 \rangle = S\left(\mathbf{Q} = \frac{2\pi}{L}\mathbf{n}\right)$$

and assigning phases at random in the interval $(0, 2\pi)$. The resulting maps include fluctuations only from wavenumbers $l > 2\pi/L$. Hence the shape of the correlation function will differ for these realizations from the forms shown in Fig. 5 since we have effectively applied a high pass filter. However, those characteristics of the radiation field which only depend upon local properties, e.g. the abundance of hotspots and coldspots, are unaffected by the filter. Large-scale simulations over the entire sky could be generated by using the spherical harmonic expansion, equation (2.3). This is computationally demanding if the map is to resolve small-scale patterns. Unless otherwise stated, the simulations described in this section were produced by evaluating FFTs on a 512×512 grid.

A grey-scale picture of the temperature fluctuations, corresponding to a smoothing angle $\theta_s = 1$ arcmin, is shown in Plate 1 for the $h = 0.75$ scale-invariant adiabatic CDM model. Contour plots generated with a smoothing angle $\theta_s = 5$ arcmin for the total and polarization fluctuations in the adiabatic and isocurvature $h = 0.75$ models are shown in Fig. 8. Solid contours show $\nu = 1$, 2 and 3 positive thresholds and dotted contours show the corresponding negative thresholds.

The textural features discussed in Section 3 are evident in Plate 1 and the contour plots: high peaks are more highly clustered, the contour regions are significantly elongated, and the characteristic size of the small-scale structure is the coherence angle θ_c. Also, the statistically averaged shape of the hotspots described by equation (3.7) can be seen to fall off more steeply than the correlation functions given in Section 4.1. Such maps illustrate clearly the effects that beam smearing and beam switching have. In particular, experiments with switching angles smaller than the coherence angle (e.g. Uson & Wilkinson 1984a, b for which $\theta = 4.5$ arcmin) measure only the small differences of temperature associated with the gentle slope of the structure.

The number of hot and cold maxima in these realizations is compared in Table 2 with the predictions of the average number that should occur in maps of this size using the expression for $n_{\max}(\nu_t)$ obtained in Section 3. Note that we have computed γ for these two models by restricting the sums in equation (4.15) to $l > 36$ to account for the high pass filter used in the simulations. The high pass filtering affects σ_0, but not σ_1 and σ_2, thus γ is modified, but θ_* is not. Both parameters are influenced by the low pass filtering associated with the beam smearing (Fig. 6). The spectral parameters for the total intensity maps of Fig. 8 are $\sigma_0 = 1.3 \times 10^{-5}$, $\gamma = 0.474$ and $\theta_* = 8.3$ arcmin for the adiabatic case and $\sigma_0 = 6.1 \times 10^{-5}$, $\gamma = 0.397$ and $\theta_* = 13.2$ arcmin for the isocurvature case. The parameters for the polarization maps are unaffected by the high pass filter and may be read

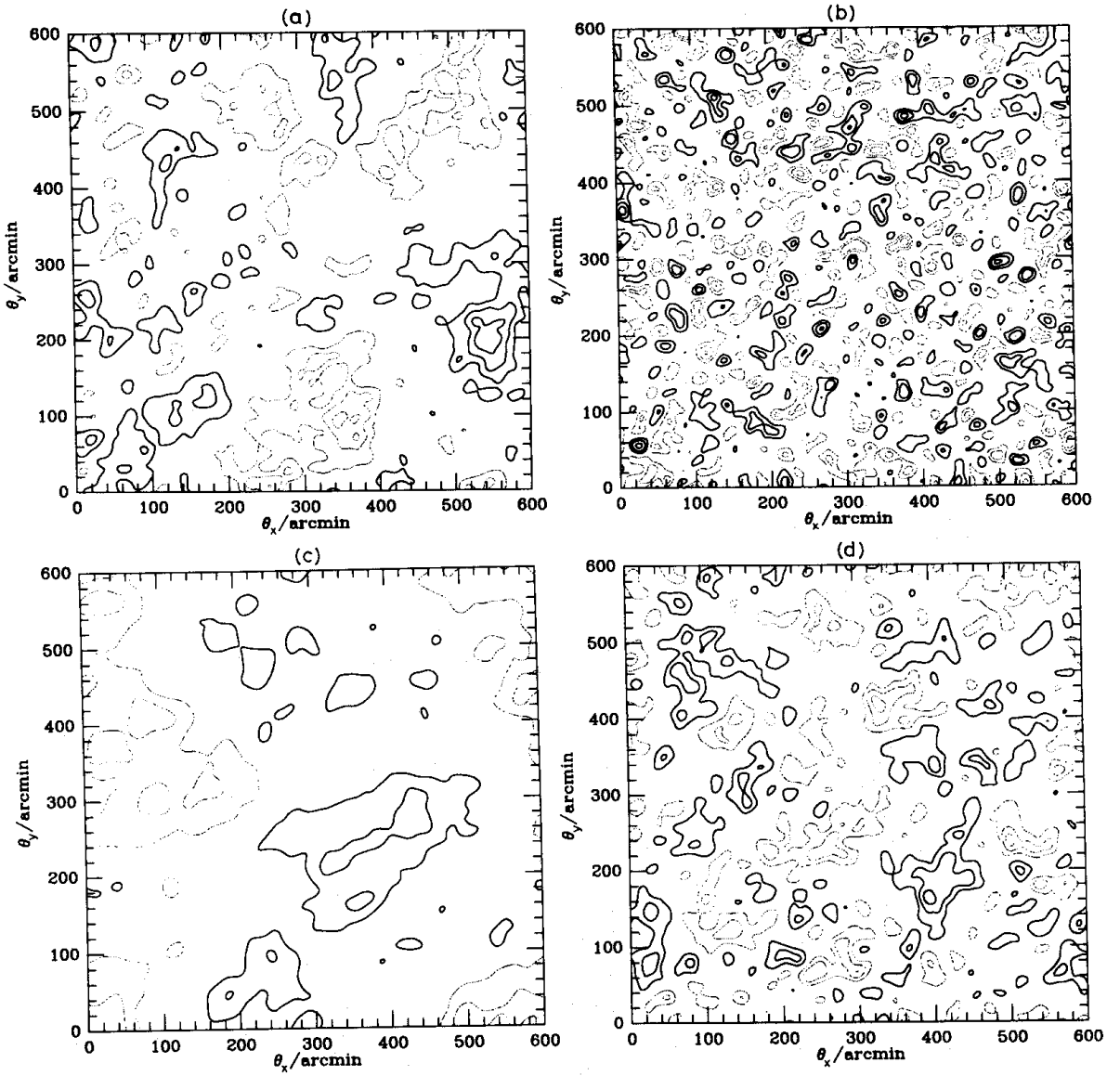

Figure 8. Realization of the Gaussian temperature and polarization fluctuations constructed using the method described in Section 5. (a, b) Show maps of the total and polarization fluctuations respectively for the $h=0.75$ scale-invariant adiabatic CDM model. (c, d) Show analogous maps for the $h=0.75$ scale-invariant isocurvature model. In constructing these plots, we used a 512×512 grid and a smoothing angle of $\theta_s=5$ arcmin. The heavy contours correspond to $\nu=1$, 2 and 3 upward fluctuations and the light lines show equivalent contours for the downward fluctuations.

from Fig. 6. The agreement of the peak numbers in Table 2 with the average number expected from the integral of equation (A1.9) is extremely good for the polarization maps since there is little power on large scales to give large map-to-map variations. The expected dispersion from equation (3.9) is significantly larger for the total intensity fluctuations, and this is reflected in the deviations of the counted numbers from the theoretical means. This is especially important for the isocurvature model. In this case, the large amount of clustering on the scale of the map implies a large dispersion which is reflected in the distribution of ΔN_{pk} being skewed towards negative values, with occasional large positive excursions, as we have verified by explicit construction of a number of realizations.

For the adiabatic map shown in Plate 1, equation (3.4) predicts $(22\,\text{arcmin})^2$ of the map should be $>3\sigma_0$ in height, giving an average area per contour region of $(9.5\,\text{arcmin})^2$. The trend of

Table 2. Number densities of peaks in 10 degree square simulations of the radiation field compared with theory.

	$\nu_{max}(\nu)$ adiabatic						$\nu_{max}(\nu)$ isocurvature					
	total			pol			total			pol		
ν	theory	max	min	theory	max	min	theory	max	min	theory	max	min
3.0	2.7	3	4	10	8	12	0.8	0	0	3.6	1	3
2.0	27	19	32	87	85	92	8.7	8	7	33	36	38
1.0	106	95	92	268	281	269	37	37	23	118	117	124
0.0	197	187	191	385	392	390	74	69	51	200	196	207
−1.0	233	217	232	404	418	415	92	79	72	225	225	241
−2.0	238	225	238	404	418	415	95	83	78	227	226	242

Notes

Columns labelled theory give the theoretically expected total number of maxima (or minima) derived from equation (A1.9). Columns labelled max give the total number of maxima counted above the indicated threshold for each realization shown in Fig. 8 and the columns labelled min list the number of minima counted. The columns labelled total give results for the total intensity fluctuation maps (Fig. 8a and c) and those labelled pol show results for the polarization maps (Fig. 8b and d).

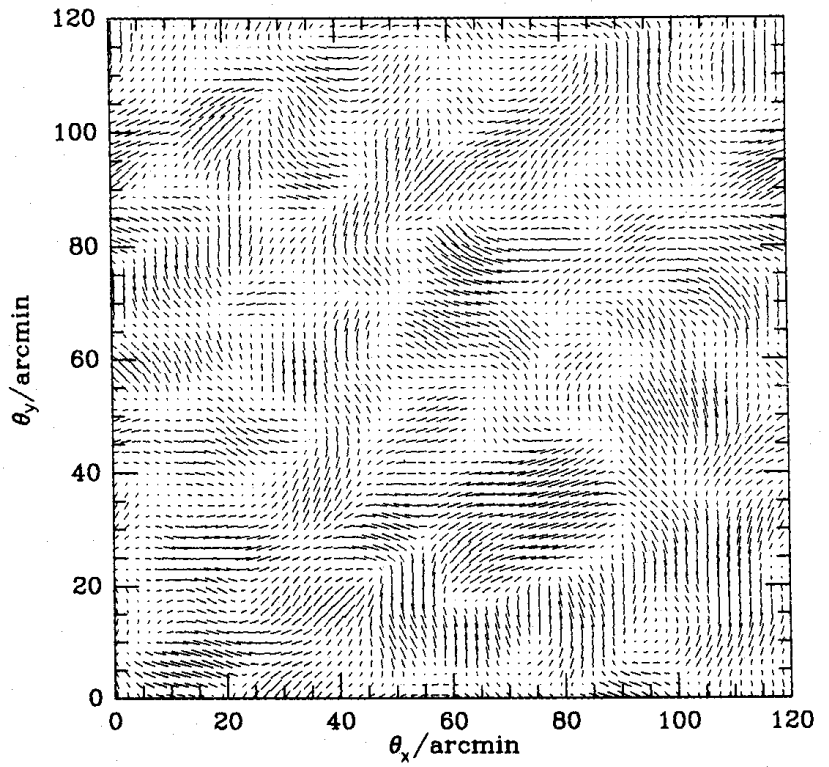

Figure 9. Simulation of the degree and spatial variation of the plane of polarization in a 2°×2° patch for the $h=0.75$ adiabatic model simulated in Fig. 8. The length of each vector is proportional to the degree of polarization and the orientation gives the plane of polarization. This picture was constructed on a 128×128 grid using a smoothing angle of $\theta_s=1$ arcmin. For visual clarity, we only plot 64×64 vectors.

decreasing size of contour regions with increasing threshold is also evident in this plot. The separation between $3\sigma_0$ hotspots and $-3\sigma_0$ coldspots in Plate 1 should be about 100 arcmin using equation (3.5).

In Fig. 9 we show a map of the degree and orientation of the linear polarization fluctuations expected in the $h=0.75$ adiabatic CDM model. This particular simulation was constructed on a

128×128 grid following the procedure outlined in Appendix 5. The smoothing scale is 1 arcmin. Notice that the characteristic size of the domains over which the polarization direction is coherent is $\sim\theta_{cp}$. It may be possible to set constraints on CDM models using small-beam polarization experiments since these do not require beam switching (see Efstathiou 1987).

6 Discussion

In this paper we have presented detailed calculations of the radiation fluctuations expected in scale-invariant CDM models and we have provided general formulae to describe some of the spatial characteristics of the radiation pattern. Past anisotropy experiments have generally been of the beam-switching type (Partridge 1987, to be published) in which the expectation value of the temperature differences measured in two or three beams may be related to differences of $C(0;\theta_s)-C(\theta;\theta_s)$. For this type of experiment our results may easily be used to predict the variances expected in CDM models for any value of θ_s. The analysis of more complicated experiments, e.g. drift-scan observations, requires specific predictions for $C(\theta)$ in order to set constraints of any particular theory. This latter type of experiment which makes more use of the spatial structure in $C(\theta)$ is potentially more powerful, particularly if the spatial characteristics of confusion or instrumental noise differs from that expected in the model.

The key feature of scale-invariant radiation fluctuations is the slow decline of $C(\theta)$, characterized by the relatively large coherence angles. Experiments probing angular scales $>\theta_c$ are therefore preferred to optimize the signal from primordial fluctuations. For experiments at $\lambda\sim1$ cm this means using horns or perhaps a close-packed array of small dishes (Lasenby, private communication). In either case, it is quite likely that some sort of map of the sky fluctuations will be produced. Indeed low-resolution maps have already been constructed using the balloon-borne observations of the Princeton and Berkeley groups (e.g. Lubin & Villela 1986) and the Soviet satellite *Prognoz 9* (Strukov & Skulachev 1984). The most important use of such maps will be direct estimation of $C(\theta)$. Power spectrum analysis is an alternative way of analysing the map. However the power spectra coefficients $C_{obs}(l)$ computed for incomplete patches of the sky are not statistically independent and thus the main advantage over correlation function analysis is lost (Peebles 1973). For practical applications the significance levels associated with measures of $C(\theta)$ or $C_{obs}(l)$ will most likely be estimated by Monte Carlo simulations in which many realizations similar to Fig. 8 (or their spherical harmonic generalizations) are generated for a specific theoretical model. This procedure will undoubtedly be necessary in the analysis of interferometric data where the sensitivity to different Fourier components will be related in a complex way to the spatial distribution of the array.

In principle, maps could also be used to obtain σ_0, γ, θ_* and other spatial characteristics from the statistics of hotspots and coldspots. However, we believe that the most useful aspect of the statistical formulae for Gaussian random fields that we have derived in Section 3 lies in the physical insight they provide for the texture of the radiation fluctuations expected in any cosmological scenario with Gaussian initial conditions. This is not without practical applications since the properties of hotspots and coldspots, such as their number densities, characteristic sizes and shapes, offer an important consistency check of Gaussian models. For example, it would be a remarkable coincidence if confusion sources had the same characteristics as the primordial hotspots and coldspots whilst also having a $C_{obs}(\theta)$ compatible with a CDM model. Using the formulae given in Section 3 and the related appendices one can quickly check whether the features in a map are compatible with a Gaussian model. The importance of these tests, and others that can be constructed numerically using Monte Carlo simulations, is that they provide redundancy checks of both the underlying statistical distribution and form of the radiation fluctuations.

We have also demonstrated the machinery required to make accurate computations of the radiation power spectrum and autocorrelation functions and how these may be used to construct realizations of the radiation field. At this stage in the search for CMB anisotropies it is difficult to make more specific theoretical computations of direct relevance to realistic experiments. However, the simulation technique is easily applicable to complex experimental configurations where analytic calculations would be impractical. By comparing such Monte Carlo calculations with real data, the likelihood of a given theoretical model can be assessed.

We hope that the parameters for the CDM models presented in Table 1 will serve as a challenge for prospective experimenters. The predicted anisotropies in these models are not beyond reach given well-designed experiments. Indeed scale-invariant isocurvature models are already probably excluded by large-angle anisotropy limits (EB). If the limits can be improved sufficiently to exclude the current favourite adiabatic CDM model ($h \approx 0.5$, $\Omega_B \approx 0.1$), we will be forced to considerable revision of our views on the origin of galaxies and perhaps of conditions in the early Universe.

Acknowledgments

JRB's research was supported by an Alfred P. Sloan Fellowship, a Canadian Institute for Advanced Research Fellowship and the NSERC of Canada. GE thanks the Institute for Advanced Study for their hospitality while some of this work was completed.

References

Abramowitz, M. & Stegun, I. A. (eds), 1970. *Handbook of Mathematical Functions,* Dover Publications, New York.
Axenides, M., Brandenberger, R. & Turner, M. S., 1983. *Phys. Lett.*, **126B,** 178.
Bardeen, J. M., Steinhardt, P. J. & Turner, M. S., 1983. *Phys. Rev. D,* **28,** 679.
Bardeen, J. M., Bond, J. R., Kaiser, N. & Szalay, A. S., 1986. *Astrophys. J.*, **304,** 15.
Blumenthal, G. R., Faber, S. M., Primack, J. R. & Rees, M. J., 1984. *Nature,* **311,** 517.
Bond, J. R. & Efstathiou, G., 1984. *Astrophys. J.*, **285,** L45.
Bond, J. R. & Szalay, A. S., 1983. *Astrophys. J.*, **274,** 443.
Chandrasekhar, S., 1960. *Radiative Transfer,* Dover Publications, New York.
Davis, M. & Peebles, P. J. E., 1983. *Astrophys. J.*, **267,** 465.
Davis, M., Efstathiou, G., Frenk, C. S. & White, S. D. M., 1985. *Astrophys. J.*, **292,** 371.
Doroshkevich, A. G., Zel'dovich, Ya. B. & Sunyaev, R. A., 1978. *Sov. Astr.*, **22,** 523.
Efstathiou, G., 1987. In: *Cosmology, Astronomy and Fundamental Physics, Proc. Second ESO/CERN Symp.*, p. 103, eds Setti, G. & van Hove, L., ESO Publications, Garching bei München.
Efstathiou, G. & Bond, J. R., 1986. *Mon. Not. R. astr. Soc.*, **218,** 103.
Fischler, W., Ratra, B. & Susskind, L., 1985. *Nucl. Phys.*, **B259,** 730.
Guth, A. & Pi, S.-Y., 1982. *Phys. Rev. Lett.*, **49,** 1110.
Halliwell, J. J. & Hawking, S., 1985. *Phys. Rev. D.*, **31,** 1777.
Kaiser, N., 1983. *Mon. Not. R. astr. Soc.*, **202,** 1169.
Kaiser, N., 1984. *Astrophys. J.*, **282,** 374.
Lubin, P. & Villela, T., 1986. In: *Galaxy Distances and Deviations from the Hubble Flow,* p. 169, eds Madore, B. F. & Tully, B. F., Reidel, Dordrecht, Holland.
Melchiorri, F., Melchiorri, B. O., Ceccarelli, C. & Pietranera, L., 1981. *Astrophys. J.*, **250,** L1.
Ostriker, J. P. & Vishniac, E. T., 1986. *Astrophys. J.*, **306,** L51.
Peebles, P. J. E., 1968. *Astrophys. J.*, **153,** 1.
Peebles, P. J. E., 1973. *Astrophys. J.*, **185,** 413.
Peebles, P. J. E. & Yu, J. T., 1970. *Astrophys. J.*, **162,** 815.
Sazhin, M. V., 1985. *Mon. Not. R. astr. Soc.*, **216,** 25P.
Starobinskii, A., 1982. *Phys. Lett.*, **117B,** 175.
Strukov, I. A. & Skulachev, D. P., 1984. *Sov. Ast. Lett.*, **10,** 1.
Uson, J. M. & Wilkinson, D. T., 1984a. *Astrophys. J.*, **277,** L1.
Uson, J. M. & Wilkinson, D. T., 1984b. *Nature,* **312,** 427.

Vittorio, N. & Silk, J., 1984. *Astrophys. J.*, **285,** L39.
White, S. D. M., Frenk, C. S. & Davis, M., 1983. *Astrophys. J.*, **274,** L1.
Wilson, M. L., 1982. *Astrophys. J.*, **253,** L53.
Wilson, M. L., 1983. *Astrophys. J.*, **273,** 2.
Wilson, M. L. & Silk, J., 1981. *Astrophys. J.*, **243,** 14.
Yang, J., Turner, M. S., Steigman, G., Schramm, D. N. & Olive, K. A., 1984. *Astrophys. J.*, **281,** 493.
Zabotin, N. A. & Nasel'skii, P. D., 1985. *Sov. Astr.*, **29,** 614.

Appendix 1: Densities of maxima and minima for 2D gaussian fields

In this appendix, we sketch the derivation of the peak density of 2D homogeneous, isotropic Gaussian random fields. We follow the techniques and notation of BBKS.

The peak density is the 'operator'

$$n_{\rm pk}=\sum_p \delta(\hat{q}-\hat{q}_p)=|\det(\zeta)|\,\delta(\boldsymbol{\eta}). \tag{A1.1}$$

Here, $\boldsymbol{\eta}=\nabla F$ and the ζ_{ij} are the components of the second derivative matrix. We use an orthogonal set of coordinates in the two-sphere in the following. We rotate to the principal axes of ζ_{ij}, by angle θ, to the diagonal form $-\mathrm{diag}\,(\lambda_1,\lambda_2)$, ordered by $\lambda_1\geq\lambda_2$, and introduce the variables

$$x=(\lambda_1+\lambda_2)/\sigma_2, \qquad e=(\lambda_1-\lambda_2)/(2\sigma_2 x), \tag{A1.2}$$

in terms of which

$$\zeta_{11}=-\frac{\sigma_2 x}{2}[1+2e\cos(2\theta)],\ \zeta_{22}=\frac{\sigma_2 x}{2}[1-2e\cos(2\theta)]. \qquad \zeta_{12}=-\sigma_2 x e\sin(2\theta). \tag{A1.3}$$

Since the principal axes are oriented, π is the maximum rotation angle required to transform the ζ system into the principal axes system. [This restriction enters as a constraint on the probability distribution, equation (A1.6), below.] The transformation of the volume element in ζ-space is

$$d\zeta_{11}\,d\zeta_{22}\,d\zeta_{12}=2\sigma_2^3 x^2\,dx\,e\,de\,d\theta. \tag{A1.4}$$

To obtain the probability distribution involving the variables x, e, and θ, we transform the Gaussian distribution obtained with the ζ_{ij}. The result is simplified if we use the variable

$$w=(\nu-\gamma x)/(1-\gamma^2)^{1/2} \tag{A1.5}$$

in place of ν, so that w and x are independent, and $\langle w^2\rangle=1$. The distribution is then

$$P(\nu,\boldsymbol{\eta},x,e,\theta)\,dw\,dx\,de\,d\theta=\exp(-w^2/2)\frac{dw}{(2\pi)^{1/2}}\exp(-x^2/2)\frac{dx}{(2\pi)^{1/2}}\exp(-\boldsymbol{\eta}^2/\sigma_1^2)$$
$$\times\frac{d^2\boldsymbol{\eta}}{\pi\sigma_1^2}\exp(-4x^2e^2)\,8x^2\,e\,de\frac{d\theta}{\pi}. \tag{A1.6}$$

The orientation angle, θ, is thus randomly distributed over $0\leq\theta<\pi$. The mean differential density of maxima is

$$\mathcal{N}_{\rm max}(\nu_0,x_0,e_0,\theta_0)=\langle\delta(\nu-\nu_0)\,\delta(\boldsymbol{\eta})\,\delta(x-x_0)\,\delta(e-e_0)\,\delta(\theta-\theta_0)\,\sigma_2^2x^2(1-4e^2)\,\vartheta(1-2e)\,\vartheta(e)\rangle. \tag{A1.7}$$

The average is taken using the distribution, equation (A1.6), ϑ is the Heaviside unit function which expresses the constraints required to satisfy $\lambda_1\geq\lambda_2\geq0$.

Integration over the orientation angle, θ, yields $\mathcal{N}_{\max}(\nu, x, e)\, d\nu\, dx\, de$, which can be inferred from equation (A2.3) of Appendix 2. A subsequent integration over e gives the differential density

$$\mathcal{N}_{\max}(\nu, x)\, d\nu\, dx = \frac{1}{2\pi\theta_*^2} \exp(-\nu^2/2) \frac{d\nu}{(2\pi)^{1/2}} g(x, \gamma, x_*)\, dx,$$

$$g(x, \gamma, x_*) \equiv f(x) \frac{\exp[-(x-x_*)^2/2(1-\gamma^2)]}{[2\pi(1-\gamma^2)]^{1/2}},$$

$$f(x) \equiv x^2 - 1 + \exp(-x^2). \tag{A1.8}$$

The integration over x from 0 to ∞ can also be done analytically, unlike in the 3D case:

$$\mathcal{N}_{\max}(\nu)\, d\nu = \frac{1}{2\pi\theta_*^2} \exp(-\nu^2/2) \frac{d\nu}{(2\pi)^{1/2}} G(\gamma, \gamma\nu),$$

$$G(\gamma, x_*) \equiv (x_*^2 - \gamma^2)\left[1 - \frac{1}{2}\operatorname{erfc}\left\{\frac{x_*}{[2(1-\gamma^2)]^{1/2}}\right\}\right] + x_*(1-\gamma^2)\frac{\exp\{-x_*^2/[2(1-\gamma^2)]\}}{[2\pi(1-\gamma^2)]^{1/2}}$$

$$+ \frac{\exp[-x_*^2/(3-2\gamma^2)]}{(3-2\gamma^2)^{1/2}}\left[1 - \frac{1}{2}\operatorname{erfc}\left\{\frac{x_*}{[2(1-\gamma^2)(3-2\gamma^2)]^{1/2}}\right\}\right]. \tag{A1.9}$$

The high ν limit, $G \to \gamma^2(\nu^2 - 1)$. For $\nu < 0$, use should be made of $\operatorname{erfc}(-x) = 2 - \operatorname{erfc}(x)$.

Integration over ν from some (sharp) threshold ν_t to ∞ gives $n_{\rm pk}(\nu_t)$, which must be evaluated numerically. However, certain calculations can be done analytically which give accurate approximations to this integrated number density. For example, the total number of peaks of arbitrary height is

$$n_{\rm pk}(-\infty) = (4\pi\sqrt{3})^{-1}\theta_*^{-2} = (4.665\theta_*)^{-2}. \tag{A1.10}$$

The differential number density of minima, $\mathcal{N}_{\min}(\nu) = \mathcal{N}_{\max}(-\nu)$, can be combined with the differential number density of maxima via

$$(\mathcal{N}_{\max} + \mathcal{N}_{\min})(\nu)\, d\nu = \frac{\gamma^2}{2\pi\theta_*^2} \frac{\exp(-\nu^2/2)}{(2\pi)^{1/2}} \left\{\nu^2 - 1 + \frac{\exp[-x_*^2/(3-2\gamma^2)]}{\gamma^2(3-2\gamma^2)^{1/2}}\right\} \tag{A1.11}$$

to yield the analytic expression for the integrated (minimum plus maximum) density

$$n_{\max}(\nu_t) + n_{\min}(\nu_t) = \frac{\gamma^2}{(2\pi)^{3/2}\theta_*^2}\nu_t \exp(-\nu_t^2/2) + \frac{1}{4\pi\sqrt{3}\theta_*^2}\operatorname{erfc}\left\{\frac{\nu_t}{[2(1-2\gamma^2/3)]^{1/2}}\right\}. \tag{A1.12}$$

Fig. 1(c) shows that if we use equation (A1.12) but impose an upper limit using equation (A1.10), we have a reasonably accurate approximation for $n_{\max}(\nu_t)$ which is very accurate for $\gamma\nu > 0.5$.

The mean number density of upcrossing points on the contour surfaces of height ν_t is given by

$$n_{\rm up}(\nu_t) = \langle \delta(F - \nu_t\sigma_0)\, |\eta_2|\, \vartheta(\eta_2)\, \delta(\eta_1)\, |\zeta_{11}| \rangle$$

$$= \frac{\gamma^2}{(2\pi)^{3/2}\theta_*^2} \exp(-\nu_t^2/2)\left\{|\nu_t|[1 - \operatorname{erfc}(|a\nu_t|/2)] + \frac{(2/a)}{(2\pi)^{1/2}} \exp[-(a\nu_t)^2/2]\right\},$$

$$a^2 \equiv (2\gamma^2/3)/(1 - 2\gamma^2/3). \tag{A1.13}$$

The Euler characteristic of the contour surfaces per unit volume is

$$n_\chi(\nu_t)=\langle\delta(F-\nu_t\sigma_0)\,|\,\eta_2|\,(-\zeta_{11})\,\delta(\eta_1)\rangle$$
$$=2\frac{\gamma^2}{(2\pi)^{3/2}\,\theta_*^2}\exp(-\nu_t^2/2)\,\nu_t. \tag{A1.14}$$

These approximations to $n_{\max}(\nu_t)$ are also indicated in Fig. 1(c). Equation (A1.12) is more accurate down to lower ν_t.

[The evaluation of these formulae is aided by the introduction of the variable

$$b=-\left(\frac{2/3}{1-2\gamma^2/3}\right)^{1/2}(2\zeta_{11}/\sigma_2+\gamma\nu)$$

obeying the relations $\langle b^2\rangle=1$, $\langle b\nu\rangle=0$. The required probability distribution,

$$P(\nu,b,\boldsymbol{\eta})\,d\nu\,db\,d^2\boldsymbol{\eta}=\exp(-\nu^2/2)\frac{d\nu}{(2\pi)^{1/2}}\exp(-b^2/2)\frac{db}{(2\pi)^{1/2}}\exp(-\boldsymbol{\eta}^2/\sigma_1^2)\frac{d^2\boldsymbol{\eta}}{\pi\sigma_1^2},$$

is then just a product of independent distributions. The presence of the δ-functions in equations (A1.13) and (A1.14) simplifies the integrations leading to the closed form results given.]

Appendix 2: The shapes of 2D maxima and minima

The conditional probabilities for the local shape parameters x and e characterizing the Taylor series expansion of the field

$$F(\varpi)\approx\nu\sigma_0-\tfrac{1}{4}\sigma_2 x\varpi^2[1+2e\cos(2\theta)] \tag{A2.1}$$

follow from some of the results obtained along the way to the derivation of the number density of maxima described in Appendix 1. The distribution of x subject to the constraint that the peak has height ν is

$$P_x(x\,|\,\nu)\,dx=\frac{\mathcal{N}_{\max}(\nu,x)}{\mathcal{N}_{\max}(\nu)}dx=\frac{g(x,\gamma,\gamma\nu)}{G(\gamma,\gamma\nu)}dx, \tag{A2.2}$$

where g and G are defined in Appendix 1.

The distribution of 'ellipticity' e subject to the constraint of given x – it is independent of ν – is

$$P_e(e\,|\,\nu,x)=\frac{8x^4}{f(x)}(1-4e^2)\exp(-4x^2e^2)\,ede. \tag{A2.3}$$

The ellipticity is restricted to lie in the range $0\le e\le 0.5$. It is more conventional to discuss shapes in terms of the principal axial ratios a_1 and a_2, where $\lambda_2/\lambda_1=a_1^2/a_2^2$, or in terms of the eccentricity. The distribution of the eccentricity,

$$\varepsilon\equiv(1-\lambda_2/\lambda_1)^{1/2}\equiv 2[e/(1+2e)]^{1/2}, \tag{A2.4}$$

is a simple transformation of equation (A2.3):

$$P_\varepsilon(\varepsilon\,|\,\nu,x)\,d\varepsilon=\frac{8x^4}{f(x)}\frac{4(1-\varepsilon^2)\,\varepsilon^3\,d\varepsilon}{(2-\varepsilon^2)^5}\exp\left[-\left(\frac{x\varepsilon^2}{2-\varepsilon^2}\right)^2\right]. \tag{A2.5}$$

As in the 3D case, one should choose x using equation (A2.2) and e or ε using equations (A2.3) or (A2.5). It is also possible to integrate over the x to form $\mathcal{N}_{\max}(\nu,e)\,d\nu\,de$, hence the

conditional probability

$$P_e(e|\nu) \equiv \mathcal{N}_{\max}(\nu, e)/\mathcal{N}_{\max}(\nu)$$
$$= \frac{(1-4e^2)\,8ede}{[1+8(1-\gamma^2)\,e^2]^{1/2}} \frac{\exp(-4x_*^2e^2)}{G(\gamma, x_*)} \left\{1-\frac{1}{2}\,\mathrm{erfc}\left[\frac{x_*}{\{2(1-\gamma^2)[1+8(1-\gamma^2)\,e^2]\}^{1/2}}\right]\right\}. \tag{A2.6}$$

This probability density can be transformed to a constrained eccentricity distribution $P_\varepsilon(\varepsilon|\nu)$ using equation (A2.4) to convert from e to ε.

Following the methods given in appendix 4 of BBKS, we derive the distribution of shapes $F(\varpi)$ given that at $\varpi=0$ there is a peak characterized by the constraint data $\mathscr{C}=\{\nu, x, e, \theta\}$. The distribution is Gaussian with mean

$$\langle F(\varpi)|\mathscr{C}\rangle = \frac{\nu}{1-\gamma^2}[\langle F(\varpi)\,\nu\rangle - \gamma\langle F(\varpi)\,x\rangle] + \frac{x}{1-\gamma^2}[\langle F(\varpi)\,x\rangle - \gamma\langle F(\varpi)\,\nu\rangle] + 8xe\langle F(\varpi)\,xe\rangle$$
$$= \sigma_0\left[\frac{\nu}{1-\gamma^2}(\psi+\nabla^2\psi/2) - \frac{(x/\gamma)}{1-\gamma^2}(\gamma^2\psi+\nabla^2\psi/2) - 4(xe/\gamma)(\psi'/r-\nabla^2\psi/2)\cos(2\theta)\right] \tag{A2.7}$$

and dispersion

$$\langle[\Delta F(\varpi)]^2|\mathscr{C}\rangle/\sigma_0^2 = 1-\frac{1}{1-\gamma^2}\psi^2 - \frac{1}{1-\gamma^2}\psi\nabla^2\psi - \frac{1}{\gamma^2(1-\gamma^2)}(\nabla^2\psi/2)^2 - \frac{1}{\gamma^2}(\psi')^2 - \frac{1}{2\gamma^2}[r(\psi'/\varpi)']^2. \tag{A2.8}$$

The radius, ϖ, is expressed in units of θ_*. The dispersion retains the same spherically symmetric form [equation (A2.8)] when the orientation angle constraint is dropped, but the mean is modified:

$$\langle F(\varpi)|\max \text{ at } \varpi=0, \nu, x, e\rangle = \text{equation (A2.7) with } e=0. \tag{A2.9}$$

The profiles are therefore spherically symmetric, as expected. The same result is obtained by explicitly angle-averaging the mean equation (A2.7). If a further averaging over ν above some threshold ν_t is performed, equation (A2.9) becomes the cross-correlation function $C_{\mathrm{pk},\Delta}$. (The factor of 4 in going from Δ_T to $\Delta T/T$ is included in this.)

Appendix 3: Distance between maxima and minima

We ignore correlations, supposing that maxima and minima are not highly correlated at their average separation. The probability that there is a minimum of depth below ν_t a distance b away from a maximum is then

$$P(b)\,db = 2b\,db/b_{\min}(\nu_t)^2, \tag{A3.1}$$

where

$$b_{\min}(\nu_t) \equiv [\pi n_{\min}(\nu_t)]^{-1/2} \tag{A3.2}$$

is the radius within which a minimum should be encountered from an ambient field point. The analogous radius for maxima is $b_{\max}(\nu_t) = b_{\min}(-\nu_t)$. (A high threshold for coldspots has $\nu_t \ll 0$.)

The mean distance of a minimum is then

$$\langle b\,|\,\mathrm{min}, \nu_t\rangle = 2b_{\mathrm{min}}(\nu_t)/3. \tag{A3.3}$$

The mean distance to a minimum of arbitrary depth is therefore

$$\langle b\,|\,\mathrm{min}, \nu_t=\infty\rangle = 1.755\,\theta_*. \tag{A3.4}$$

These estimates are exact for an arbitrary field point. However, the true distribution for minima of depth below ν_t a distance, b, away from a maximum of height in excess of ν_p involves the conditional density of minima

$$n_{\mathrm{min}}(b, \nu_t\,|\,\mathrm{max\ at}\ r=0, \nu_p) = n_{\mathrm{min}}(\nu_t)[1+C_{\mathrm{min,\,max}}(b; \nu_t, \nu_p)], \tag{A3.5}$$

where $C_{\mathrm{min,\,max}}$ is the minimum–maximum correlation function which is quite difficult to evaluate for small b. Thus equation (A3.1) is modified, becoming

$$P(b)\,db = [1+C_{\mathrm{min,\,max}}(b; \nu_t, \nu_p)]\,2b\,db/b_{\mathrm{min}}(\nu_t)^2\,\vartheta(b_1-b). \tag{A3.6}$$

The maximum value b_1 of b in this distribution is that for which $P(<b_1)=1$. Of course $b_1=b_{\mathrm{min}}$ in the uncorrelated case. Provided the maximum–minimum correlation function $C_{\mathrm{max,\,min}}(b)$ is small at the separation $\langle b\rangle$ determined using equation (A3.3), the estimate given for the average distance of minima from ambient field points will suffice for the average distance of minima from maximum points. Since $\langle b\rangle$ is only a few θ_*, where we expect that the correlation will be slightly more negative due to the coherence of the maximum, the mean separation will be slightly larger.

The mean distance from a peak of height above ν_{t2} to the next peak of height above ν_{t1} requires knowledge of the peak–peak correlation function, since the distribution is given by equation (A3.6) with $C_{\mathrm{max,\,max}}(b;\,\nu_{t1},\,\nu_{t2})$ replacing $C_{\mathrm{min,\,max}}$ and $b_{\mathrm{max}}(\nu_{t1})$ replacing b_{min}. Again, the uncorrelated estimate is a reasonable first guess.

Appendix 4: 2D peak–peak correlation function

In this appendix, we obtain the 2D correlation function of peaks in the same approximation used in BBKS: derivatives of the normalized correlation function $\psi(\varpi)=C(\theta)/C(0)$ are ignored when compared with $\psi(\varpi)$. At small angles, a local power-law approximation holds for $\psi(\varpi)$, hence ψ' and ψ'' fall off faster than ψ by θ^{-1} and θ^{-2}, respectively.

The N-point correlation function of peak number densities,

$$\left\langle \prod_i \mathcal{N}_{\mathrm{max}}(\hat{q}_i, \nu_i)\,d\nu_i \right\rangle = \left\langle \prod_i \delta[\nu_i - F(\hat{q}_i)/\sigma_0)\,d\nu_i\,|\,\lambda_1(\hat{q}_i)\lambda_2(\hat{q}_i)\,|\,\vartheta(\lambda_2(\hat{q}_i))]\,\delta[\boldsymbol{\eta}(\hat{q}_i)] \right\rangle, \tag{A4.1}$$

requires the joint probability distribution for the $5N$ variables $\{\nu_i, x_i, e_i, \theta_i, \boldsymbol{\eta}_i\}$. Even in two dimensions, the full problem is quite complicated. However, the evaluation is tractable provided we only include $\langle \nu_i \nu_j\rangle = \psi(|\,\hat{q}_i - \hat{q}_j\,|)$ in the cross-correlations, which should be valid for the class of $\psi(\varpi)$ considered here. The derivation follows precisely the steps given in BBKS. In particular, steps (A6.6)–(A6.12) of appendix 6 in that paper can be followed to yield

$$\left\langle \prod_i \mathcal{N}_{\mathrm{max}}(\hat{q}_i, \nu_i, x_i)\,d\nu_i\,dx_i \right\rangle = \prod_i \left\{ \exp(-\nu_i^2/2)\,\frac{d\nu_i}{(2\pi)^{1/2}}\,g[x_i, \gamma, x_*(i)]\,\frac{f(x_i)}{2\pi\theta_*^2}\,dx_i \right\}$$

$$\times \frac{\exp(\tilde{\nu}\,\dagger\,\mathbf{C}\tilde{\nu}/2)}{[\det(\mathbf{I}+\boldsymbol{\Psi}/\{1-\gamma^2\})]^{1/2}}, \tag{A4.2}$$

where $\tilde{\nu}$ is an N-dimensional vector with components

$$\tilde{\nu}(i) \equiv (\nu_i - \gamma x_i)/(1-\gamma^2) \tag{A4.3}$$

and

$$\mathbf{C} \equiv \left(\mathbf{I} + \frac{\boldsymbol{\Psi}}{1-\gamma^2}\right)^{-1} \boldsymbol{\Psi} \tag{A4.4}$$

and $\boldsymbol{\Psi}$ are $N \times N$ matrices. The components of the latter are

$$\boldsymbol{\Psi}_{ij} = \psi(|\hat{q}_i - \hat{q}_j|), \qquad i \neq j, \qquad \boldsymbol{\Psi}_{ij} = 0, \qquad i = j. \tag{A4.5}$$

This is equivalent to the equation (A6.13) for the 3D case of BBKS.

Integration over x requires some approximation. The prescription used in BBKS which we adopt here is to replace fg by a Gaussian,

$$f(x)\, g(x, \gamma, x_*) = f(\langle x \mid \nu \rangle)\, g(\langle x \mid \nu \rangle, \gamma, \gamma\nu) \exp\left[-\tfrac{1}{2}\beta_g(\langle x \mid \nu \rangle)(x - \langle x \mid \nu \rangle)^2\right], \tag{A4.6}$$

centred about the conditional mean

$$\langle x \mid \nu \rangle = x_* + (1-\gamma^2)\, H(\gamma, x_*)/G(\gamma, x_*),$$

where

$$H(\gamma, x_*) \equiv \partial G/\partial x_* = 2x_* \left[\left[1 - \frac{1}{2}\operatorname{erfc}\left\{\frac{x_*}{[2(1-\gamma^2)]^{1/2}}\right\}\right]\right.$$

$$- 2x_* \frac{\exp\left[-x_*^2/(3-2\gamma^2)\right]}{(3-2\gamma^2)^{3/2}} \left[\left[1 - \frac{1}{2}\operatorname{erfc}\left\{\frac{x_*}{[2(1-\gamma^2)(3-2\gamma^2)]^{1/2}}\right\}\right]\right.$$

$$\left. + 4\frac{(1-\gamma^2)^2}{3-2\gamma^2} \frac{\exp\left\{-x_*^2/[2(1-\gamma^2)]\right\}}{[2\pi(1-\gamma^2)]^{1/2}}. \right. \tag{A4.7a}$$

Asymptotically, we have

$$\langle x \mid \nu \rangle \to \gamma\nu \left[1 + \frac{2(1-\gamma^2)}{\gamma^2(\nu^2-1)}\right] \qquad \text{as } \nu \to \infty. \tag{A4.7b}$$

The dispersion of the Gaussian, β_g^{-1}, is obtained by evaluating the second derivative function

$$\beta_g(x) = -\frac{\partial^2 \ln [g(x, \gamma, x_*)]}{\partial x^2} = \frac{1}{1-\gamma^2} + \frac{2\{x^2[1-\exp(-x^2)-2x^2\exp(-x^2)]+[1-\exp(-x^2)]^2\}}{[x^2-1+\exp(-x^2)]^2} \tag{A4.8}$$

at the conditional mean, equation (A4.7a).

With this approximation, the average differential peak density becomes

$$N_{\max}(\nu)\, d\nu \approx \frac{G_{\text{app}}}{(2\pi)^{3/2}\theta_*^2} \exp(-\nu^2/2)\, d\nu,$$

where

$$G_{\text{app}} = (2\pi)^{1/2}\, g(\langle x \mid \nu \rangle, \gamma, \gamma\nu)/[\beta_g(\langle x \mid \nu \rangle)]^{1/2}. \tag{A4.9}$$

The two-point function of peaks chosen according to some selection function $t(\nu)$, which we take to be that associated with a sharp threshold ν_t, $t(\nu)=\vartheta(\nu-\nu_t)$, is given by

$$1+C_{\max,\max}(r) \equiv \langle n_{\max}(r_1;\nu_t)\, n_{\max}(r_1;\nu_t)\rangle / \langle n_{\max}(\nu_t)\rangle^2$$
$$= \frac{\int d\nu_1\, t(\nu_1)\mathcal{N}_{\max}(\nu_1) \int d\nu_2\, t(\nu_2)\,\mathcal{N}_{\max}(\nu_2) \exp\,[S(\nu_1,\nu_2,\psi)]/D(\psi)^{1/2}}{[\int d\nu\, t(\nu)\,\mathcal{N}_{\max}(\nu)]^2}. \tag{A4.10}$$

The functions S and D are related to the matrices $\mathbf{C}$ and $\beta \equiv \mathrm{diag}\,[\beta_g(1),\ldots,\beta_g(N)]$ by

$$S \equiv \hat{\nu}\dagger \mathbf{C}[\beta - \mathbf{C}\gamma^2/(1-\gamma^2)^2]^{-1}\,\beta\hat{\nu}/2,$$
$$D \equiv \det\,[\beta - \mathbf{C}\gamma^2/(1-\gamma^2)^2]/\det\,(\beta), \tag{A4.11}$$

where $\hat{\nu}$ is a vector with components

$$\hat{\nu}(i) = (\nu_i - \gamma\langle x\,|\,\nu_i\rangle)/(1-\gamma^2). \tag{A4.12}$$

Their explicit form is therefore

$$S(\nu_1,\nu_2,\psi) \equiv \left[2\hat{\nu}_1\hat{\nu}_2 - \frac{(\hat{\nu}_1^2+\hat{\nu}_2^2)\,\psi}{(1-\gamma^2)} + \frac{[\hat{\nu}_1^2/\beta_g(2)+\hat{\nu}_2^2/\beta_g(1)]\,\gamma^2\psi}{(1-\gamma^2)^2}\right]\alpha\psi/[2D(\psi)],$$

$$D(\psi) \equiv 1 + \frac{[\beta_g^{-1}(1)+\beta_g^{-1}(2)]\,\alpha\gamma^2\,\psi^2}{(1-\gamma^2)^3} - \frac{\beta_g^{-1}(1)\,\beta_g^{-1}(2)\,\alpha\gamma^4\,\psi^2}{(1-\gamma^2)^4},$$

$$\alpha \equiv [1-\psi^2/(1-\gamma^2)^2]^{-1}. \tag{A4.13}$$

In computing the integrals in equation (A4.10), the approximation, equation (A4.9), must be used in both numerator and denominator.

In the small ψ limit, we have

$$1+C_{\max,\max}(\varpi) \approx \exp\,[\langle\tilde{\nu}\rangle^2\psi(\varpi)], \tag{A4.14}$$

where the average of $\tilde{\nu}$ is taken with respect to ν and x:

$$\langle\tilde{\nu}\rangle \equiv \frac{\int d\nu\, t(\nu)\,\mathcal{N}_{\max}(\nu)\,\hat{\nu}}{\int d\nu\, t(\nu)\,\mathcal{N}_{\max}(\nu)}. \tag{A4.15}$$

Appendix 5: Polarization statistics

The distribution function for polarized radiation is a 2×2 matrix $f_{\lambda\lambda'}(\mathbf{x},\mathbf{q},\tau)$, where the index λ refers to the two polarization states $\hat{\varepsilon}_\lambda$ of the electromagnetic waves incident from direction $-\hat{q}$. Analogous to the introduction of Δ_T in Section 2.1, we introduce $\Delta_{\lambda\lambda'}$ to describe the fluctuations in the polarization matrix. The conventional Stokes parameters, I, Q, U, V, are related to this matrix by an expansion in Pauli spin matrices,

$$(\Delta_{\lambda\lambda'}) = \tfrac{1}{2}(s_0 I + \mathbf{s}\cdot\boldsymbol{\sigma}),$$
$$s_0 = I = \Delta_T, s_1 = U, s_2 = V, s_3 = Q. \tag{5.1}$$

If Thomson scattering is the only process modifying the geodesic propagation of the photons, then the transfer problem for the polarization matrix considerably simplifies (Chandrasekhar

1960). For a given plane wave, the polarization matrix is diagonal if the unit vectors

$$\hat{\varepsilon}_l(\mathbf{k}, \hat{q}) = \frac{\hat{k} - \mu \hat{q}}{(1-\mu^2)^{1/2}}, \qquad \hat{\varepsilon}_r(\mathbf{k}, \hat{q}) = \hat{k} \times \hat{q} \tag{A5.2}$$

are used to describe the polarization vectors. In this case, the only non-zero Stokes parameters are I and $Q = \Delta_P$. We solve our transfer equations relative to this polarization basis (Kaiser 1983; BE) since $\Delta_{\lambda\lambda'}$ remains diagonal as propagation proceeds. However, when we reconstruct the polarization distribution at the present time by summing over wavenumbers, we must first rotate our k-dependent basis to a fixed basis $\hat{e}_i(\hat{q})$ in the plane perpendicular to the photon direction $\hat{q}$: $\hat{\varepsilon}_l = R(\phi_k)\,\hat{e}_1$, $\hat{\varepsilon}_r = R(\phi_k)\,\hat{e}_2$, where R is a 2D matrix describing rotation by an angle ϕ_k. In this new basis the polarization matrix is $(\Delta_{ij}) = R\dagger(\Delta_{\lambda\lambda'})\,R$, hence there are now three non-zero Stokes parameters, the total intensity $I = \Delta_T(\hat{q})$, and the two polarization measures

$$Q(\hat{q}) = \frac{V_x}{(2\pi)^3} \int d^3k\, \Delta_P(k, \mu, \tau_0) \cos(2\phi_k),$$

$$U(\hat{q}) = \frac{V_x}{(2\pi)^3} \int d^3k\, \Delta_P(k, \mu, \tau_0) \sin(2\phi_k). \tag{A5.3}$$

Clearly, Q and U are independent 2D Gaussian random fields with zero means and covariance functions

$$\langle Q(\hat{q})\, Q(\hat{q}') \rangle = \langle U(\hat{q})\, U(\hat{q}') \rangle = \tfrac{1}{2} C_P(\theta), \qquad \cos(\theta) = \hat{q} \cdot \hat{q}'. \tag{A5.4}$$

To construct small-angle maps of the polarization it is a good approximation to assign angles $\phi_{\mathbf{n}}$ uniformly at random in the interval $[0, 2\pi]$ and to generate two maps by evaluating the Fourier series

$$Q(\boldsymbol{\theta}) = \sum_{n_x, n_y} D_P(\mathbf{n}) \cos(2\phi_{\mathbf{n}}) \exp\left[i \frac{2\pi}{L} \mathbf{n} \cdot \boldsymbol{\theta} \right],$$

$$U(\boldsymbol{\theta}) = \sum_{n_x, n_y} D_P(\mathbf{n}) \sin(2\phi_{\mathbf{n}}) \exp\left[i \frac{2\pi}{L} \mathbf{n} \cdot \boldsymbol{\theta} \right]. \tag{A5.5}$$

The amplitude $D_P(\mathbf{n})$ is chosen from a Gaussian distribution with zero mean and variance

$$\langle |D_P(\mathbf{n})|^2 \rangle = (1/2)\, S_P\left(\mathbf{Q} = \frac{2\pi}{L} \mathbf{n} \right) \approx (1/2)\, C_{Pl},$$

and the same set of amplitudes and phases of D_P are used in generating the two maps. In the plot of the polarization vectors shown in Fig. 9, the length of each vector is proportional to $[Q^2(\boldsymbol{\theta}) + U^2(\boldsymbol{\theta})]^{1/2}$ and the orientation is given by $2\phi = \tan^{-1}(U/Q)$.